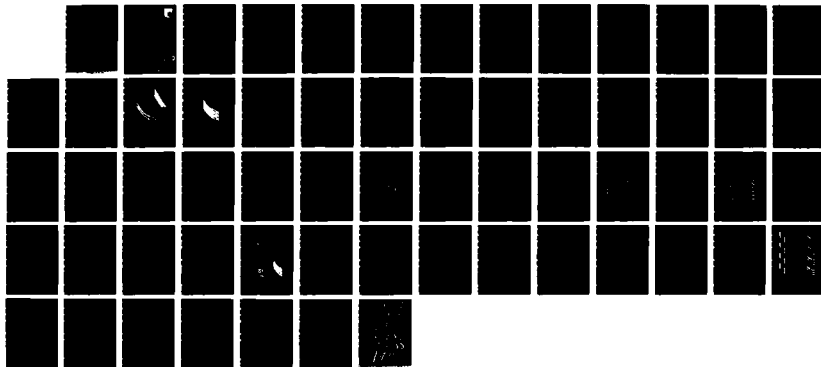


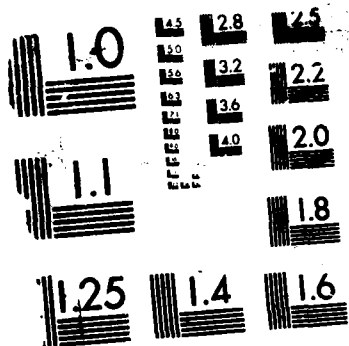
RD-A188 284 NUMERICAL SIMULATION OF UNSTEADY FLOW IN A COMPRESSOR 1/1
ROTOR CASCADE(U) DAYTON UNIV OH RESEARCH INST
J W SCOTT NOV 86 UDR-TR-86-27 AFWAL-TR-86-2863

UNCLASSIFIED F33615-83-K-2318

F/G 28/4

NL





MICROCOPY RESOLUTION TEST CHART

DTIC FILE COPY



AD-A188 284

AFWAL-TR-86-2063

NUMERICAL SIMULATION OF UNSTEADY FLOW IN A
COMPRESSOR ROTOR CASCADE

James N. Scott

University of Dayton
Research Institute
300 College Park
Dayton, Ohio 45469

November 1986

Final Report for Period January 1984 - February 1986

Approved for public release; distribution unlimited.

DTIC
S ELECTED NOV 24 1987 D
H

AERO PROPULSION LABORATORY
AIR FORCE WRIGHT AERONAUTICAL LABORATORIES
AIR FORCE SYSTEMS COMMAND
WRIGHT-PATTERSON AIR FORCE BASE, OHIO 45433-6563

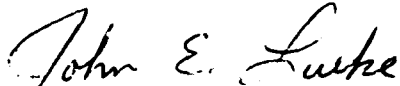
87 11 14 080

NOTICE

When Government drawings, specifications, or other data are used for any purpose other than in connection with a definitely related Government procurement operation, the United States Government thereby incurs no responsibility nor any obligation whatsoever; and the fact that the government may have formulated, furnished, or in any way supplied the said drawings, specifications, or other data, is not to be regarded by implication or otherwise as in any manner licensing the holder or any other person or corporation, or conveying any rights or permission to manufacture use, or sell any patented invention that may in any way be related thereto.

This report has been reviewed by the Office of Public Affairs (ASD/PA) and is releasable to the National Technical Information Service (NTIS). At NTIS, it will be available to the general public, including foreign nations.

This technical report has been reviewed and is approved for publication.



JOHN E. LUEKE
Compressor Research Group
Technology Branch
Turbine Engine Division

FOR THE COMMANDER



MICHAEL E. STEFKOVICH, Maj, USAF
Deputy Director
Turbine Engine Division
Aero Propulsion Laboratory



FRANCIS R. OSTDIEK
Chief, Technology Branch
Turbine Engine Division
Aero Propulsion Laboratory

"If your address has changed, if you wish to be removed from our mailing list, or if the addressee is no longer employed by your organization please notify AFRL/TI, W-PAFB, OH 45433 to help us maintain a current mailing list".

Copies of this report should not be returned unless return is required by security considerations, contractual obligations, or notice on a specific document.

UNCLASSIFIED

SECURITY CLASSIFICATION OF THIS PAGE

A105284

REPORT DOCUMENTATION PAGE

1a. REPORT SECURITY CLASSIFICATION Unclassified		1b. RESTRICTIVE MARKINGS									
2a. SECURITY CLASSIFICATION AUTHORITY		3. DISTRIBUTION/AVAILABILITY OF REPORT Approved for public release; distribution unlimited.									
2b. DECLASSIFICATION/DOWNGRADING SCHEDULE											
4. PERFORMING ORGANIZATION REPORT NUMBER(S) UDR-TR-86-27		5. MONITORING ORGANIZATION REPORT NUMBER(S) AFWAL-TR-86-2063									
6a. NAME OF PERFORMING ORGANIZATION University of Dayton Research Institute	6b. OFFICE SYMBOL (If applicable)	7a. NAME OF MONITORING ORGANIZATION Air Force Wright Aeronautical Laboratories Aero Propulsion Laboratory (AFWAL/POTX)									
6c. ADDRESS (City, State and ZIP Code) 300 College Park Dayton, Ohio 45469-0001		7b. ADDRESS (City, State and ZIP Code) Wright-Patterson Air Force Base, Ohio 45433-6563									
8a. NAME OF FUNDING/SPONSORING ORGANIZATION Air Force Wright Aeronautical Laboratories	8b. OFFICE SYMBOL (If applicable) AFWAL/POTX	9. PROCUREMENT INSTRUMENT IDENTIFICATION NUMBER F33615-83-K-2318									
8c. ADDRESS (City, State and ZIP Code) Wright-Patterson Air Force Base, Ohio 45433-6563		10. SOURCE OF FUNDING NOS. <table border="1"><tr><th>PROGRAM ELEMENT NO.</th><th>PROJECT NO.</th><th>TASK NO.</th><th>WORK UNIT NO.</th></tr><tr><td>62203F</td><td>ILIR</td><td>P3</td><td>07</td></tr></table>		PROGRAM ELEMENT NO.	PROJECT NO.	TASK NO.	WORK UNIT NO.	62203F	ILIR	P3	07
PROGRAM ELEMENT NO.	PROJECT NO.	TASK NO.	WORK UNIT NO.								
62203F	ILIR	P3	07								
11. TITLE (Include Security Classification) Numerical Simulation of Unsteady Flow in a Compressor Rotor Cascade		14. DATE OF REPORT (Yr., Mo., Day) 1986 November									
12. PERSONAL AUTHOR(S) Scott, James N.		15. PAGE COUNT 53									
16. SUPPLEMENTARY NOTATION											

17. COSATI CODES <table border="1"><tr><th>FIELD</th><th>GROUP</th><th>SUB. GR.</th></tr><tr><td>21</td><td>01</td><td></td></tr></table>	FIELD	GROUP	SUB. GR.	21	01		18. SUBJECT TERMS (Continue on reverse if necessary and identify by block number) compressor rotor, Navier-Stokes equations, numerical simulation, unsteady flow		
FIELD	GROUP	SUB. GR.							
21	01								

19. ABSTRACT (Continue on reverse if necessary and identify by block number) Unsteady flow in a two-dimensional compressor rotor is computed by solving the time-dependent compressible Navier-Stokes equations for flow between two adjacent rotor blades. The computations are carried out on a CDC Cyber 845 computer and a CRAY XMP computer using MacCormack's explicit finite difference scheme. The primary objective of this program is to numerically simulate the rotor flow field accounting for the effects of wakes from the upstream stator and inlet guide vane. Particular attention is focused on the influence of unsteady effects on the mass flow rate, shock structure, and shock wave-boundary layer interaction. <i>(Key words): -</i>		
---	--	--

20. DISTRIBUTION/AVAILABILITY OF ABSTRACT UNCLASSIFIED/UNLIMITED <input type="checkbox"/> SAME AS RPT. <input checked="" type="checkbox"/> DTIC USERS <input type="checkbox"/>		21. ABSTRACT SECURITY CLASSIFICATION Unclassified
22a. NAME OF RESPONSIBLE INDIVIDUAL Dr. Art J. Wennerstrom		22b. TELEPHONE NUMBER (Include Area Code) (513) 255-7163
		22c. OFFICE SYMBOL AFWAL/POTX

PREFACE

This work was conducted under Contract F33615-83-K-2318 with the Aero Propulsion Laboratory, Wright-Patterson Air Force Base, Ohio. The authors would like to thank the Air Force Technical Monitor, Dr. A. J. Wennerstrom, for providing the rotor design data and background information as well as significant insight into the problem.

Accession For	
NTIS GRA&I	<input checked="" type="checkbox"/>
DTIC TAB	<input type="checkbox"/>
Unannounced	<input type="checkbox"/>
Justification	
By -	
Distribution/	
Availability Codes	
Avail and/or	Special
A-1	



TABLE OF CONTENTS

<u>Section</u>		<u>Page</u>
I	INTRODUCTION	1
II	ANALYSIS	5
	A. GOVERNING EQUATIONS	5
	B. GRID SYSTEM	6
	C. BOUNDARY CONDITIONS	7
	D. INITIAL CONDITIONS	17
	E. TURBULENCE MODEL	19
III	NUMERICAL PROCEDURE	22
IV	DISCUSSION OF RESULTS	25
V	CONCLUSIONS AND RECOMMENDATIONS	48
	REFERENCES	50
	NOMENCLATURE	52

LIST OF ILLUSTRATIONS

<u>Figure</u>		<u>Page</u>
1	Compressor rotor blade geometry	4
2	Rotor mesh	8
3	Extended grid for multiple blade passages	9
4	Boundary conditions	11
5	Time varying total pressure profile at leading edge of blade passage	15
6	Computed results at time $T = .785 \times 10^{-3}$ seconds (8.328 characteristic times) with steady characteristic variables at the inflow boundary	26
7	Comparison of time-dependent mass flow and steady state mass flow at blade leading edge- laminar velocity vectors for turbulent computation	29
8	Comparison of time-dependent mass flow and steady state mass flow at blade leading edge- turbulent calculation	29
9	Velocity vectors for laminar computation	30
10	Velocity vectors for turbulent computation	30
11	Mach contours for laminar computation	32
12	Mach contours for turbulent computation	32
13	Blade surface pressure variation with time: laminar case	33
14	Blade surface pressure variation with time: turbulent case	35
15	Stagnation pressure for laminar computation	36
16	Stagnation pressure for turbulent computation	36

LIST OF ILLUSTRATIONS (CONCLUDED)

<u>Figure</u>		<u>Page</u>
17	a. Typical computed mach number contours. Laminar, steady inflow boundary condition test case	38
	b. Typical computed static pressure contours. Laminar, steady inflow boundary condition test case	38
	c. Typical computed stagnation pressure contours. Laminar, steady inflow boundary condition test case	38
	d. Typical computed velocity vectors. Laminar, steady inflow boundary condition test case	38
18	Mass flow rate at blade leading edge. Steady inflow boundary conditions	39
19	Computed mass flow rate as a function of exit nozzle area ratio	41
20	Computed stagnation pressure ratio as a function of exit nozzle area ratio	42
21	Variation in stagnation pressure area ratio as a function of mass flow rate	43
22	Computed mass flow rate. Steady and unsteady inflow boundary conditions	44
23	Computed mach numbers at several characteristics times. Time-dependent inflow boundary conditions	46
24	Computed static pressure contours at several characteristic times. Time-dependent inflow boundary conditions	46
25	Computed stagnation pressure contours at several characteristic times. Time-dependent inflow boundary conditions	47

SECTION I INTRODUCTION

The transonic compressor has played a significant role in the development of modern aircraft propulsion systems. It is a major component in virtually all modern high-speed aircraft engines currently in use. Much time and effort has been directed toward research into the fluid dynamics of transonic compressors to gain a better understanding of the complex flow phenomena which are produced by the rotating machinery.

However, analysis of unsteady flow in turbomachinery continues to be one of the most difficult and challenging problems in internal flows. In a supersonic or transonic compressor the relative Mach number of the flow entering the blade passage is supersonic while its axial component remains subsonic. As a result of the supersonic relative flow entering the blades, a complex system of shock and expansion waves is present in the blade passage. The presence of these waves along with their interaction with the viscous flow in the boundary layer results in performance degradation. In addition, these features are influenced by the unsteady flow due to the wakes from upstream stators and an inlet guide vane. To achieve a better understanding of the interaction between the unsteady and viscous-inviscid effects in the compressor, the use of the time-dependent compressible Navier-Stokes equations is necessary.

In recent years significant progress has been achieved in the numerical simulation of unsteady flow in turbomachinery. Recently Mitchell¹ and Hodson² have extended Denton's method³ to investigate the unsteady inviscid interaction of upstream wakes on a moving blade row. To simulate the unsteady flow entering the computational domain Hodson formulated inflow boundary conditions in which he specified the stagnation temperature (assumed constant in the wake relative reference frame), the relative flow angle (α), and the mass flow per unit area (ρu). The wake is accounted

for by moving a velocity profile containing the wake defect across the inflow boundary at the relative blade speed.

Janssens and Hirsch have utilized finite element methods to treat boundary conditions in developing a procedure for computing viscous-inviscid interactions in cascades, accounting for large separated boundary layer regions and correcting for Coriolis and centrifugal effects on turbulence.⁴ Calvert⁵ has also developed a viscous-inviscid interaction method based on Denton's time marching technique to investigate the steady flow in several transonic compressor cascades. His results show the presence of strong shock waves and regions of separated flow for certain configurations.

There has also been progress toward the solution of the time-dependent viscous flow in turbomachinery components. Patched and overlaid grids have been developed for use in conjunction with the thin-layer Navier-Stokes equations to simulate very low-speed, unsteady flow in an axial turbine configuration.⁶ The current contract has been directed toward the analysis of time-dependent flow in a supersonic compressor rotor.⁷ This analysis accounts for the unsteady flow produced by wakes from the upstream stator and inlet guide vane by specifying the stagnation pressure profile at the inflow boundary. This stagnation pressure profile which is obtained from experimental data, is used to develop boundary conditions based on characteristic variables. With this formulation the unsteady behavior occurs in the form of an entropy wave where entropy is one of the characteristic variables. This formulation also accounts for the velocity defect in the wakes from the upstream stator and inlet guide vane. The downstream boundary condition is based on the concept of a boundary region which incorporates a throat or choke point as a means of controlling the back pressure at the trailing edge of the blades. This approach permits the use of the "non-reflective" supersonic outflow boundary conditions at the outflow plane while allowing the unsteady fluctuations to occur more naturally in the subsonic flow at the trailing edge of the blades.

An additional objective of this effort is to obtain improved resolution of the viscous-inviscid interaction and in particular to more accurately model the unsteady behavior on the suction surface of the blades. To accomplish this, the Baldwin-Lomax algebraic eddy-viscosity turbulence model is incorporated into the computational procedure in regions near the blade surfaces. The implementation of the turbulence model also required that grid refinement be performed placing more grid points in the boundary layer regions.

The computations for the present work are performed for a stream surface at approximately 90 percent of the blade span of a high-performance transonic compressor rotor being developed in the AFWAL Aero Propulsion Laboratory at Wright-Patterson Air Force Base. The blade geometry for this rotor is shown in Figure 1. The computation accounts for a streamtube contraction of about 38 percent through the blade passage. (The current results are compared with those from previous computations and qualitatively with experimental observations.)

To more accurately simulate the periodic behavior of the flow entering the rotor, the computational domain has been expanded to compute the flow through four adjacent blades (three blade passages). This configuration was selected because it closely approximates the correct ratio of rotor blades to upstream stator blades. In this particular compressor the rotor contains 74 blades and the upstream stator contains 54 blades. The computational arrangement corresponds to the ratio of four rotor blades to three upstream stator blades. Simulation of the rotor exactly would require computing the flow through at least half of the rotor (37) blades for which adequate computer storage is not available. This configuration permits a more thorough examination of mass flow fluctuations which is the primary objectives of this program.

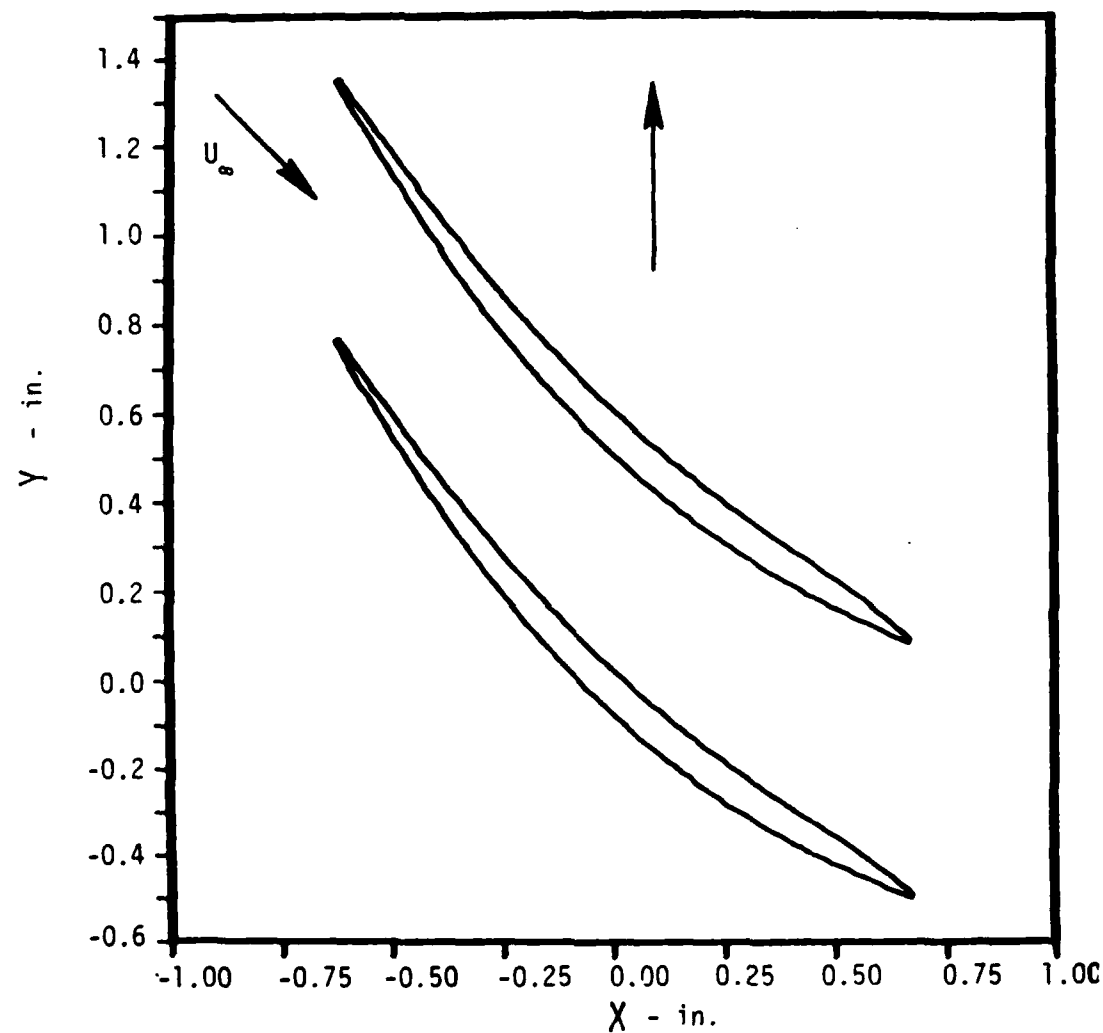


Figure 1. Compressor rotor blade geometry.

SECTION II
ANALYSIS

A. GOVERNING EQUATIONS

Since the flow in a supersonic compressor rotor contains complex viscous-inviscid interactions including shock waves, boundary layers, flow separation and unsteady phenomena, a numerical solution of the Navier-Stokes equations is required to accurately simulate the flow behavior. Thus, the complete time-dependent compressible Navier-Stokes equations are solved using an adaptation of a computer code developed by Shang^{8,9}. Variations of this code have been applied successfully for internal flows in ducts¹⁰, thus it seems appropriate for the present application. The governing equations are written in two-dimensional rectangular Cartesian coordinates as

$$\vec{U}_t + \frac{1}{\delta} \begin{pmatrix} \zeta_x \\ \zeta_y \end{pmatrix} \left(\frac{\partial \vec{E}}{\partial \zeta}, \frac{\partial \vec{F}}{\partial \zeta} \right) + \begin{pmatrix} \eta_x \\ \eta_y \end{pmatrix} \left(\frac{\partial \vec{E}}{\partial n}, \frac{\partial \vec{F}}{\partial n} \right) = 0 \quad (1)$$

where the dependent variables are given by

$$\vec{U} = \begin{bmatrix} \rho \\ \rho u \\ \rho v \\ \rho e \end{bmatrix} \quad (2)$$

The flux vectors are the Cartesian components of the continuity, momentum, and energy equations.

$$\vec{E} = \begin{bmatrix} \delta \rho u \\ \delta \rho u^2 - \sigma_{xx} \\ \delta \rho uv - \tau_{xy} \\ \delta \rho ue - \delta u \sigma_{xx} - v \tau_{xy} - q_x \end{bmatrix} \quad (3)$$

$$\vec{F} = \begin{bmatrix} \rho v \\ \rho u v - \tau_{xy} \\ \rho v^2 - \sigma_{yy} \\ \rho v e - v \sigma_{yy} - u \tau_{xy} - q_y \end{bmatrix} \quad (4)$$

The components of the stress tensor are given by

$$\sigma_{xx} = (2\mu + \lambda) \frac{\partial u}{\partial x} + \lambda \frac{\partial v}{\partial y} - p \quad (5)$$

$$\sigma_{yy} = (2\mu + \lambda) \frac{\partial v}{\partial y} + \lambda \frac{\partial u}{\partial x} - p \quad (6)$$

$$\tau_{yx} = \tau_{xy} = \mu \left(\frac{\partial u}{\partial y} + \frac{\partial v}{\partial x} \right) \quad (7)$$

$$q_x = k \frac{\partial T}{\partial x} \quad (8)$$

$$q_y = k \frac{\partial T}{\partial y} \quad (9)$$

$$\delta = \text{streamtube contraction factor } 1 - \sum_{n=1}^4 a_n x^n.$$

Expressed in this form minor deviations in flow area due to contraction in the third dimension may be approximated. Sutherland's viscosity equation, the equation of state, and the Prandtl number are specified to close the system of equations.

B. GRID SYSTEM

To optimize numerical resolution and simplify the boundary conditions the governing equations are transformed to a body oriented coordinate system. Equation (1) is expressed in the transformed coordinates where the transformation is given by

$$\zeta = \zeta(x, y)$$

$$\eta = \eta(x, y)$$

where the transformed coordinate $n = 0$ line represents the upper surface of the lower blade and the $n = JL$ line is the last row above the upper surface of the upper blade. In the streamwise direction the transformed coordinate $\zeta = 0$ line is the inflow boundary and the $\zeta = KL$ line is the outflow boundary. The two-dimensional grid is established between two adjacent rotor blades and is extended upstream to a point near the trailing edge of the upstream stator and downstream to a point well beyond the leading edge of the trailing stator. However, the downstream stator is not actually included. The grid boundaries extending upstream of the leading edge are tangent to the upper surface while the grid boundaries extending downstream of the trailing edge are tangent to the lower surface. The grid points are clustered adjacent to the boundaries which contain the blade surfaces in order to achieve the necessary resolution of the flow field in the boundary layer regions. This clustering is produced by an exponential stretching function with a controlling exponent k as described in Reference 8.

A coarse finite difference mesh for the rotor cascade is shown in Figure 2. The actual grid consists of 60 points in the streamwise direction and 46 points in the transverse or tangential direction. The grid has been expanded to include four blades. A coarse mesh for this configuration is shown in Figure 3.

C. BOUNDARY CONDITIONS

One of the primary objectives of this program is to develop boundary conditions which will account for the time-dependent effects at the inflow boundary. To achieve this, different formulations of boundary conditions were first examined for the steady flow situation. The flow enters the cascade with a supersonic relative velocity but has a subsonic axial component. The flow at the downstream boundary is subsonic. Thus, the boundary conditions required for the problem to be well posed consist of three at the inflow boundary and one at the outflow

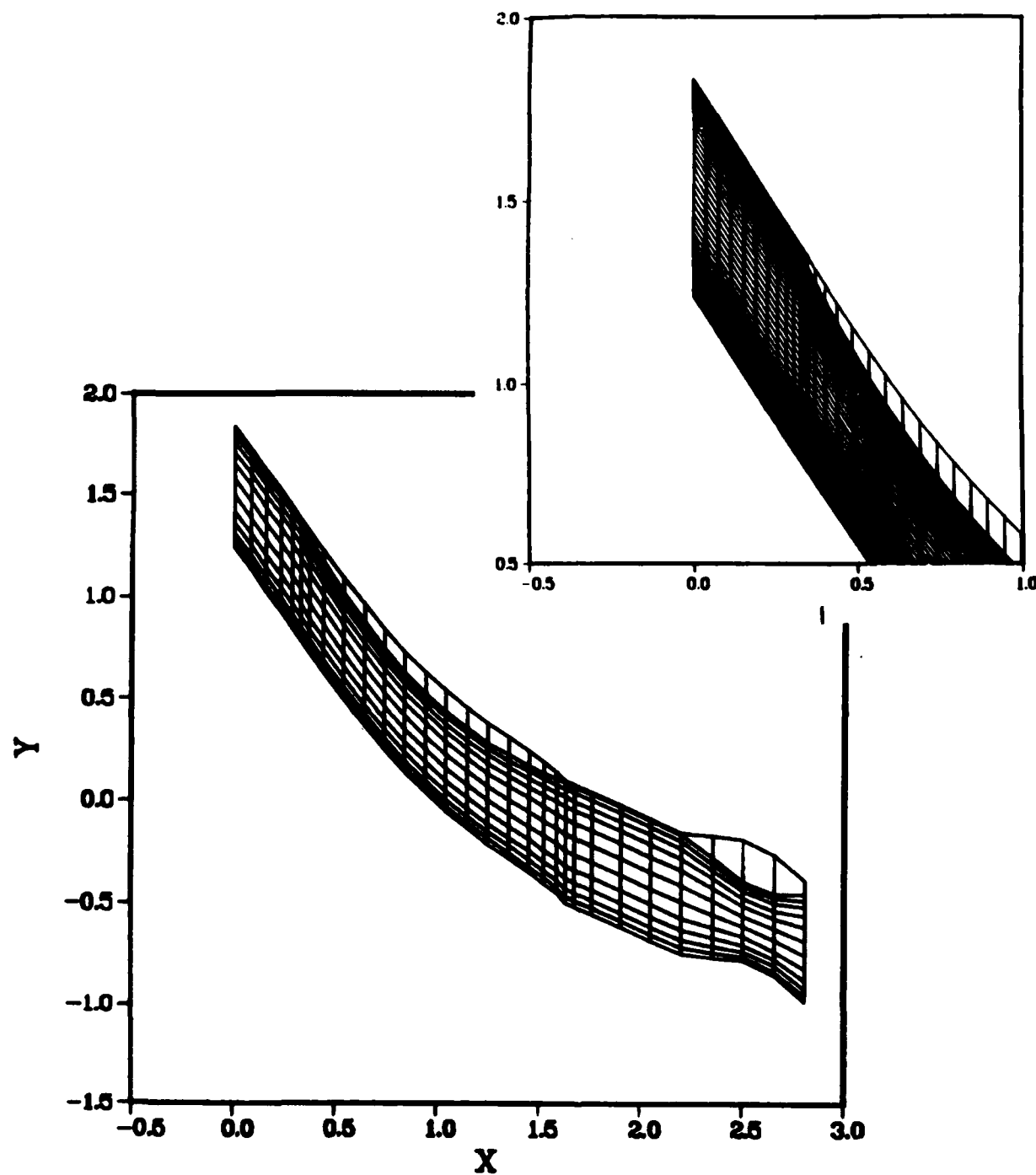


Figure 2. Rotor mesh.

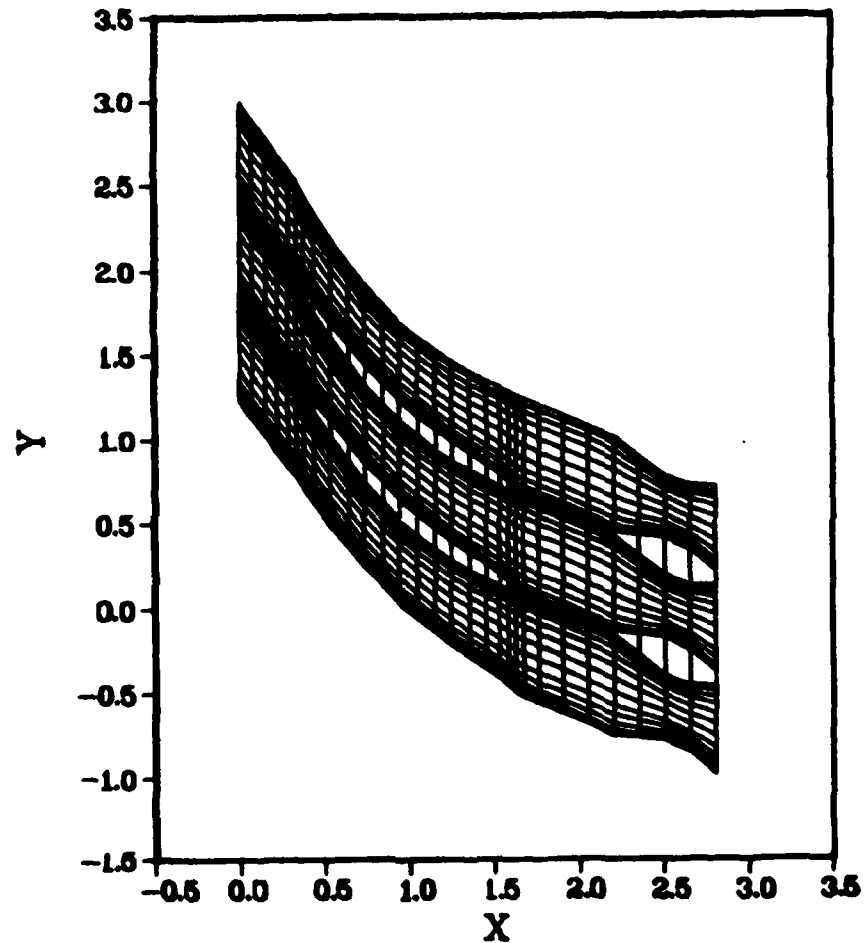


Figure 3. Extended grid for multiple
blade passages.

boundary.^{8,9,11} For this flow situation, a complex system of Mach waves and shock waves forms at the blade leading edge. Specifically, expansion waves form on the suction surface of the blade at the leading edge and propagate upstream into the incoming flow. (This alters the flow direction and velocity and the resulting flow is treated as Prandtl-Meyer flow.) As described in References 3, 7, 12, and 13, the flow entering the rotor must be periodic from one blade passage to the next and as a result of the expansion waves propagating upstream, a unique relationship exists between the inlet Mach number and incoming flow angle. This unique incidence relationship establishes a unique mass flow which must be accurately predicted since small errors in the mass flow result in incorrect angles of attack and off-design performance penalties. For these flow conditions, common practice has been to specify the stagnation pressure, stagnation temperature, and relative wheel speed at the inflow boundary while specifying static pressure at the outflow boundary.^{1,13,14} In addition to these boundary conditions, periodic boundary conditions are imposed on the boundaries extending upstream and downstream of the blades. This is necessary to satisfy the unique incidence condition upstream and to achieve the desired wake behavior downstream of the blade surfaces. Finally, the blade surface boundary conditions consist of no slip, and a prescribed wall temperature. The compatibility condition is satisfied by setting the normal pressure gradient equal to zero at the wall. These conditions are shown in Figure 4.

A formulation of the inflow and outflow boundary conditions has been developed based upon the use of characteristic variables in accordance with the procedure described by McKenna, Graham and Hankey in Reference 15. As Shang⁸ notes, the total number of required boundary conditions for the inflow and outflow boundaries is the same as the number of characteristic variables in the system of governing equations. Ideally, we would like to apply the upstream and downstream boundary conditions at upstream and downstream infinity, respectively. However, current computer

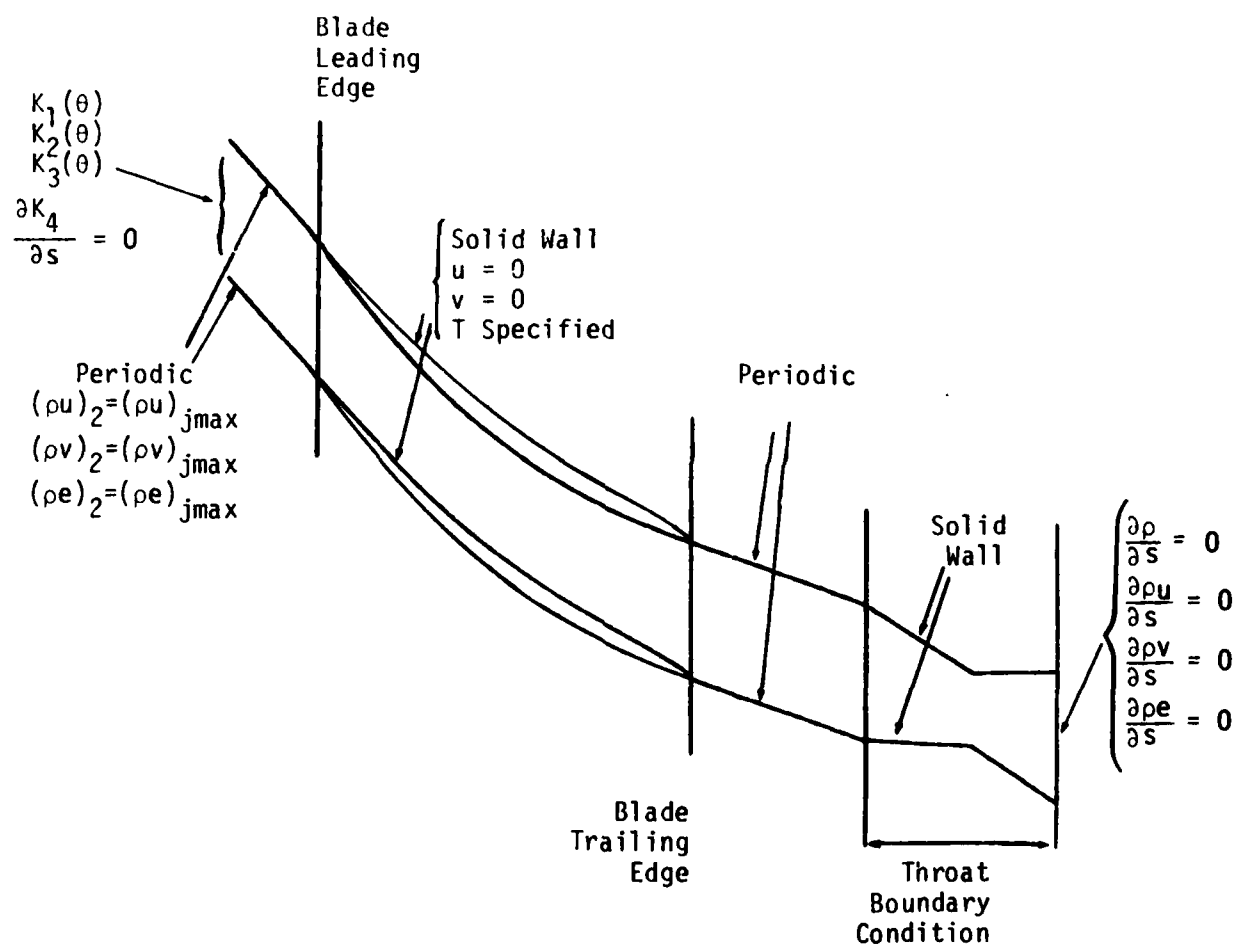


Figure 4. Boundary conditions.

storage and speed limitations dictate that the boundaries be placed immediately upstream and downstream of the region of interest. Application of these characteristic boundary conditions requires that they be placed at locations where the assumption of inviscid inflow is reasonable. In general, the characteristic variables are given by

$$K_1 = \rho - \frac{P}{c_\infty^2} \quad (10)$$

$$K_2 = v_\infty \quad (11)$$

$$K_3 = \frac{P}{\rho_\infty c_\infty} + u \quad (12)$$

$$K_4 = \frac{P}{\rho_\infty c_\infty} - u \quad (13)$$

where the ∞ subscript denotes the upstream freestream value. The nature of the problem again requires three boundary conditions upstream. At the upstream boundary, the first three characteristic variables, which represent vorticity, entropy, and the downstream running Riemann invariant, are prescribed using freestream values. These variables are then used in linear combinations with the primitive variables to write the boundary conditions in conservative variables.

For steady state inflow, the upstream conditions are

$$\rho_{1,J} = AK1 + \left(\frac{\rho_\infty}{2c_\infty} \right) \cdot \left(\frac{P_{2,J}}{\rho_\infty c_\infty} + AK3 - \frac{(\rho u)_{2,J}}{\rho_{2,J}} \right) \quad (14)$$

$$(\rho u)_{1,J} = \rho_{1,J} (0.5) \left(AK3 - \frac{P_{2,J}}{\rho_\infty c_\infty} + \frac{(\rho u)_{2,J}}{\rho_{2,J}} \right) \quad (15)$$

$$(\rho v)_{1,J} = AK2(\rho_{1,J}) \quad (16)$$

$$P_{1,J} = 0.5 \left(P_{2,J} + \rho_\infty \cdot c_\infty \left(AK3 - \frac{(\rho u)_{2,J}}{\rho_{2,J}} \right) \right) \quad (17)$$

$$(\rho e)_{1,J} = \frac{P_{1,J} + c_v}{R} + \frac{(\rho u)_{1,J}^2 + (\rho v)_{1,J}^2}{2\rho_{1,J}} \quad (18)$$

Where

$$AK1 = \rho - \frac{P}{c_\infty^2} \quad (19)$$

$$AK2 = v_\infty \quad (20)$$

$$AK3 = \frac{P_\infty}{\rho_\infty c_\infty} + u_\infty \quad (21)$$

and in general

$$P_{K,J} = \frac{R}{c_v} \left((\rho e)_{K,J} - \left(\frac{(\rho u)_{K,J}^2 + (\rho v)_{K,J}^2}{2\rho_{K,J}} \right) \right) \quad (22)$$

Implementation of these boundary conditions is intended to minimize or eliminate the influence of reflected waves which result from specifying pressure at inflow or outflow boundaries. Generally, formulations involving characteristic variables are developed for inviscid flow and have been used in inviscid flow calculations for turbomachinery.^{11,16} Since the present investigation includes viscous effects, alternative boundary conditions are required at the downstream or outflow boundary, the boundary layer and/or blade wake regions.

In addressing the unsteady flow we must remember that a complex system of shock and expansion waves is established at the leading edge of each blade. This situation is complicated further when considering the effects of the wakes from the upstream stator and inlet guide vanes. These wakes result in a velocity defect in the incoming flow which changes not only the magnitude but also the direction of the incoming velocity profile. Consequently, the strength and orientation of the wave system in each blade passage varies in a periodic fashion associated with the blade passage

frequency of the upstream stator and inlet guide vanes. The influence of the time varying inflow on the wave pattern at the inlet of the blade passage is of particular importance in compressor performance since the inlet wave pattern governs the mass flow through the compressor. We suspect that the unique incidence related to the circumferentially averaged unsteady flow is not necessarily the same as that related to an equivalent steady flow. For unsteady flow in the rotor, the characteristic boundary conditions are applied with the time-dependent inflow established by using the experimentally measured total pressure profile to define entropy, i.e., K_1 , the first characteristic variable. The total pressure in the stator depicted in Figure 5 is described by means of a Fourier-Series.

$$P_{os}(\theta) = \sum (A_n \sin n\theta + B_n \cos n\theta) \quad (23)$$

where $\theta = \frac{y}{R} - \omega t$; ω = rotation rate, R = rotor blade radius.

Additionally, the flow angle, α , exiting the stator is assumed invariant. Therefore, a relationship between P_{os} , u , p , and ρ may be obtained through the definition of total pressure.

$$\begin{aligned} P_{os} &= P \left[1 + \frac{\gamma-1}{2} \right] M_s^2 \frac{\gamma}{\gamma-1} \\ &= P \left[1 + \frac{\gamma-1}{2\gamma} \frac{\rho u^2 \sec^2 \alpha}{P} \right]^{\frac{\gamma}{\gamma-1}} \end{aligned} \quad (24)$$

From this equation density may be obtained

$$\rho = \left(\frac{2\gamma}{\gamma-1} \right) \frac{P \cos^2 \alpha}{u^2} \left[\left(\frac{P_{os}}{P} \right)^{\frac{\gamma-1}{\gamma}} - 1 \right] \quad (25)$$

and the velocity defect is accounted for by

$$u(\theta) = \cos \alpha \sqrt{\frac{2\gamma}{\gamma-1}} RT_0 \left[\left(\frac{P}{P_{os}} \right)^{\frac{\gamma-1}{\gamma}} - 1 \right]^{1/2} \quad (26)$$

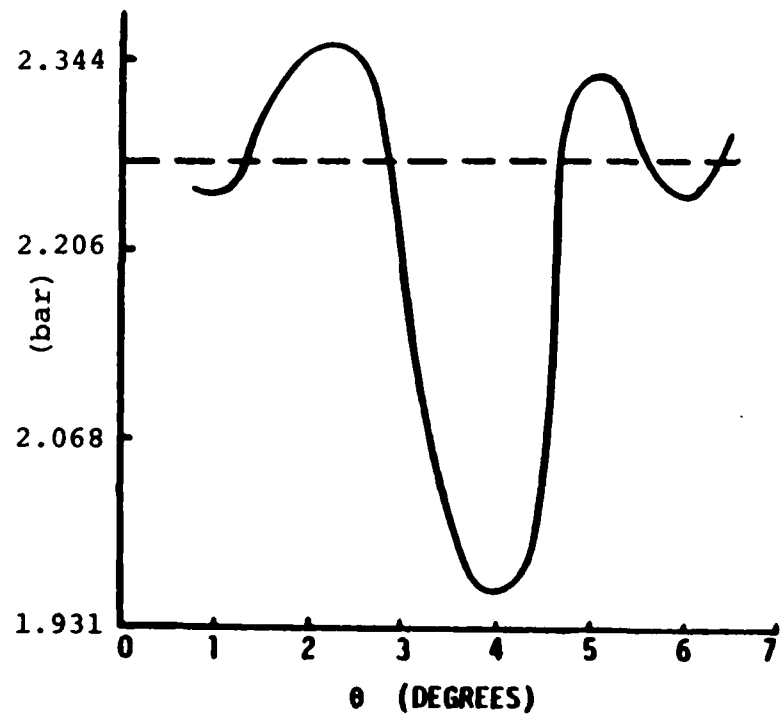


Figure 5. Time varying total pressure profile
at leading edge of blade passage.

The representation of the characteristic variables used to complete the description of the upstream boundary conditions is

$$K_1(\theta) = \frac{P_0}{\rho_0^Y} = \frac{(RT_0)^Y}{P_0^{Y-1}} ; \text{ (entropy profile)} \quad (27)$$

$$K_2(\theta) = U \tan \alpha + W ; \quad W = \text{wheel speed} \quad (28)$$

$$K_3(\theta) = \frac{P}{\rho_\infty c_\infty} + U \quad (29)$$

$$\frac{dK_4(\theta)}{dx} = 0 ; \quad K_4 = \frac{P}{\rho_\infty c_\infty} - U \quad (30)$$

This formulation differs from that used in previous studies in that the stator values of whirl velocity, static temperature and total temperature all vary with time. Although we believe that these are rational boundary conditions, time accurate experimental measurements of these quantities are required to confirm the use of these boundary conditions.

Downstream

Great difficulty has been experienced by the computational fluid dynamics (CFD) community in computing flows in short channels with subsonic outflow. This is especially true for unsteady flows in which it is intuitively unnatural to specify any flow quantity as being fixed at the outflow boundary unless that boundary is placed at downstream infinity. The difficulty was overcome in this study by inserting a convergent-divergent "second throat" at the exit. In this manner supersonic outflow may be achieved. This is known to produce no numerical difficulty. To obtain a desired downstream pressure the "second throat" area may be adjusted as follows.

Recall from shock-relationships

$$\frac{P_{t_2}}{P_{t_1}} = \frac{A_1^*}{A_2^*} \quad (31)$$

With the implementation of the "second throat" the outflow boundary conditions are simply

$$\frac{dU}{dx} = 0$$

where U is given in Equation (2).

While this approach is still not a true simulation of the downstream boundary, i.e., stator blade row, it provides a more accurate representation of the physical situation than imposing a constant variable, such as static pressure at the outflow boundary.

Lateral Boundaries

Periodic boundary conditions are imposed upstream and downstream of the leading and trailing edges of the outermost blades. At the blade surfaces no slip, and a specified wall temperature are imposed. These conditions along with the inflow and outflow boundary conditions are shown in Figure 4.

The evolution of these boundary conditions is summarized in Table 1. The formulation presented here appears to give a realistic representation of the time varying flow effects in a transonic compressor rotor. However, it must be reemphasized that time accurate experimental measurements of the proper flow quantities are essential for the verification of these boundary conditions.

D. INITIAL CONDITIONS

To start the time-dependent solution, a set of initial conditions is required for the four dependent variables at all stations. Arbitrarily, the upstream conditions were uniformly

TABLE 1. Boundary Conditions.

<u>INFLOW</u>	<u>SIDES</u>	<u>OUTFLOW</u>
(1.) Steady flow		
a.) p_0 T_0 v $\frac{\partial u}{\partial s}$ } specified	(1.) Solid walls (2.) Periodic upstream of blade (3.) Periodic upstream & downstream of blade*	(1.) p specified in in viscous region $\frac{\partial p}{\partial s} = 0$ in viscous region $\frac{\partial p}{\partial s} = 0$ $\frac{\partial pu}{\partial s} = 0$ $\frac{\partial pv}{\partial s} = 0$ $\frac{\partial pe}{\partial s} = 0$
b.) Characteristic boundary conditions		
$K_1(\theta) = \frac{p_0}{v_0}$ $K_2(\theta) = v$ $K_3(\theta) = \frac{p_{\infty}}{v_0 c_{\infty}} + u$ $K_4(\theta) = \frac{p_{\infty}}{v_0 c_{\infty}} - u$		
(2.) Unsteady Flow Characteristics		
a.) p_0 profile		
b.) Velocity defect		

New grid generation scheme
with choke point downstream
to control out flow conditions

<u>INFLOW</u>	<u>SIDES</u>	<u>OUTFLOW</u>
Unsteady flow Characteristic	Periodic upstream & between blade T.E. & choke L.E.	Supersonic with "second throat" area variation to control down- stream pressure and shock location.

prescribed everywhere as initial conditions. With these conditions numerical difficulties were observed at the downstream boundaries where periodicity was prescribed. To alleviate this problem the periodic boundary conditions were replaced with solid surfaces and the solution permitted to evolve until the flow became aligned with the channel. After approximately one characteristic time period the correct periodic boundary condition was inserted and the solution procedure continued to converge without further difficulty. Although we envision many other starting procedures, the above combination of initial conditions was used successfully in all cases reported herein.

E. TURBULENCE MODEL

The turbulence is simulated by the algebraic eddy-viscosity model developed by Baldwin and Lomax¹⁷. This turbulence model is incorporated into the computational procedure only in regions near the blade surfaces, since use of a steady flow turbulence model throughout the entire computational domain would tend to unrealistically damp the unsteady flow oscillations. The procedure used for the present calculations assumes the presence of two layers. The Prandtl-Van Driest formulation is used for the inner layer:

$$\epsilon_i = \rho l^2 |\omega| \quad (32)$$

where

$$l = k_y [1 - \exp(-y^+/A^+)]$$

$|\omega|$ is the magnitude of the vorticity:

$$|\omega| = \left| \frac{\partial u}{\partial y} - \frac{\partial v}{\partial x} \right|$$

and

$$y^+ = \left(\frac{(\rho_w |\omega_w|)}{\mu_w} \right)^{1/2} y$$

y is the distance normal to the blade surface, $A^+ = 26$ is the sublayer thickness, $k = 0.40$ is the von Karman constant, and the subscript w denotes values at the blade surfaces.

The model switches from the Van Driest formulation to the formulation for the outer region at the smallest value of y for which the inner and outer values of the eddy-viscosity are equal (i.e., $\epsilon_i \geq \epsilon_0$). The formulation for the outer layer is given by

$$\epsilon_0 = \rho K C_{cp} F_{max} y_{max} F_{KLEB} \quad (33)$$

where

$$F_{max} = y_{max} |\omega| [1 - \exp(-y^+/A^+)]$$

y_{max} is the value of y at which F_{max} occurs.

$$F_{KLEB} = [1 + 5.5 (C_{KLEB} y/y_{max})^6]^{-1}$$

and $K = 0.0168$, $C_{cp} = 1.6$, $C_{KLEB} = 0.3$.

The turbulence calculation is initiated at a streamwise location just upstream from the separation point observed in the laminar computations.¹⁴ While the incorporation of this turbulence model should give improved results, it is still inadequate for accurate prediction of the flow details. To resolve a turbulent boundary layer the first point should be within the laminar sublayer. An examination of the current results indicated that the first point from the blade surface was nominally at a y^+ of 30, which marginally meets this criteria.

The Baldwin-Lomax turbulence model was developed for steady flow computations. There is still a need for an "unsteady turbulence" model which models only the fine scale and does not suppress the large scale fluctuations which are paramount to this case.

SECTION III
NUMERICAL PROCEDURE

The flow field being investigated has a Reynolds number of 1.85×10^6 based on a blade chord. The dominant fluctuations in this case are due to the interaction of the rotor with the stator wakes. These fluctuations have a frequency of approximately 18.4K Hz, giving a characteristic time of 5.4×10^{-5} seconds. To achieve the temporal resolution for the high-frequency oscillations, MacCormack's explicit and unsplit finite difference scheme¹⁸ is appropriate for the present study. This algorithm has been used successfully for a wide range of external and internal flows involving unsteady phenomena.^{8,9,10} The computer code used in this program is a degenerate version of a three-dimensional code developed by Shang^{8,9} for operation on a vector processor. This algorithm requires a combination of alternating forward and backward differences for the predictor and corrector sweeps. This is accomplished by using a different indexing procedure for the predictor and corrector sweeps. These two steps are defined in general by:

$$\begin{aligned} U_{i,j}^{\overline{n+1}} &= U_{i,j}^n - \frac{\Delta t}{\Delta x} (E_{i+1,j}^n - E_{i,j}^n) \\ &\quad - \frac{\Delta t}{\Delta y} (F_{i,j+1}^n - F_{i,j}^n) \quad (\text{predictor}) \end{aligned} \quad (34)$$

$$\begin{aligned} U_{i,j}^{\overline{n+1}} &= 1/2 \left\{ U_{i,j}^n + U_{i,j}^{\overline{n+1}} - \frac{\Delta t}{\Delta x} (E_{i,j}^{\overline{n+1}} - E_{i-1,j}^{\overline{n+1}}) \right. \\ &\quad \left. - \frac{\Delta t}{\Delta y} (F_{i,j}^{\overline{n+1}} - F_{i,j-1}^{\overline{n+1}}) \right\} \quad (\text{corrector}) \end{aligned} \quad (35)$$

The efficiency of the code is maximized utilizing the CFL condition on allowable time increment for generalized coordinates as reported by Shang⁹:

$$\Delta t_{CFL} = 1 / \left\{ \frac{\bar{u}}{\Delta n} + \frac{\bar{v}}{\Delta \zeta} + c \left[\left(\frac{n_x}{\Delta n} + \frac{\zeta_x}{\Delta \zeta} \right)^2 + \left(\frac{n_y}{\Delta n} + \frac{\zeta_y}{\Delta \zeta} \right)^2 \right]^{1/2} \right\} \quad (36)$$

with the contravariant velocity components defined as

$$\bar{u} = \zeta_x u + \zeta_y v \quad (37)$$

$$\bar{v} = n_x u + n_y v \quad (38)$$

The range of CFL numbers used in the present investigation vary from 0.15 to as high as 0.85; although most of the calculations have been made using a CFL number of 0.8. This value seems to provide stable results in a reasonable computational time.

Numerical damping is also used in the present analysis in order to suppress numerical oscillations. Again the form of the damping terms is reported by Shang⁹. These damping or artificial viscosity terms are implemented in each sweep direction. They are:

$$\beta \Delta t \Delta n^3 \{ |\bar{u}| + (n_x^2 + n_y^2)^{1/2} c \} \frac{1}{p} \left| \frac{\partial^2 p}{\partial n^2} \right| \quad (39)$$

$$\beta \Delta t \Delta \zeta^3 \{ |\bar{v}| + (\zeta_x^2 + \zeta_y^2)^{1/2} c \} \frac{1}{p} \left| \frac{\partial^2 p}{\partial \zeta^2} \right| \quad (40)$$

In the present analysis the value of the damping constant (β) used is 2.

For steady inflow conditions the computations were performed for 6,400 time steps which corresponds to about 8.9 characteristic times based on chord length (L) divided by the upstream freestream

velocity. This required about 3.5 hours of CYBER 845 computer time. The computations using the time-dependent inflow conditions were carried out to 6,000 time steps at which point the turbulence model was implemented and the computation was continued to 11,500 time steps to ensure that a limit cycle was realized. This corresponds to about 16 characteristic times based on (L/U_∞) .

SECTION IV DISCUSSION OF RESULTS

In this investigation computations are initially performed for flow through two adjacent blades in a transonic compressor rotor, at a radial location corresponding to approximately 90 percent of the span. This rotor has a relative inflow angle of 61 degrees from the axial direction. This results in a subsonic axial velocity component having a Mach number of 0.66.

The primary goal of this program is to examine and assess the influence of unsteady flow effects on the mass flow through the compressor rotor. Two significant sources of unsteady flow are (1) the wakes from the upstream stator and inlet guide vane and (2) the oscillatory flow separation and vortex shedding on the suction surface of the blade. The wakes from the upstream blade rows enter the rotor blade passage at a well defined periodicity determined by the blade passage frequency of the rotor. The resulting unsteady flow is classified as a forced oscillation. In contrast the extent of the flow separation on the blade suction surface varies with the shedding or vortices from the blade trailing edge. This vortex shedding does not occur with the same frequency or period between subsequent vortices hence this unsteady behavior is quasi-periodic and is classified as a self-sustained oscillation.

Both of these unsteady phenomena affect the mass flow rate. In order to analyze the influence of these phenomena, computations were first performed for steady inflow boundary conditions thereby eliminating the wakes from the upstream blade rows. These computations represent laminar flow through single blade passage with attention focused on separated flow on the blade suction surface. Typical features of the flow separation with the steady inflow boundary conditions are shown in Figure 6. The presence of separated flow in such regions has been noted by other researchers in previous efforts^{4,5}. However, those investigations treated only steady flow.

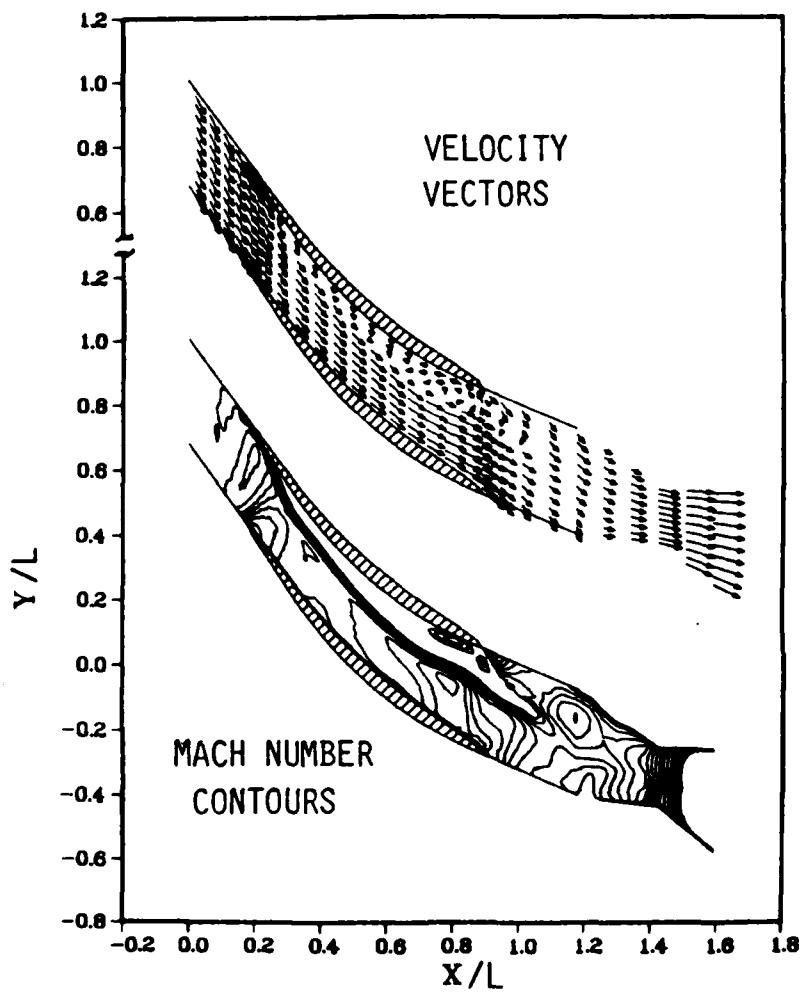


Figure 6. Computed results at time $T = .785 \times 10^{-3}$
 seconds (8.328 characteristic times)
 with steady characteristic variables
 at the inflow boundary.

Since the primary interest of the present program is on the influence of unsteady behavior on mass flow, the upstream boundary conditions were modified to account for the unsteady flow due to the wakes from the upstream blade rows. Computations were carried out for several characteristic times assuming purely laminar unsteady flow. The mass flow rate for this configuration is shown in Figure 7. This figure shows the periodic fluctuation of the mass flow which results from the wakes from the upstream blade rows. The unsteady mass flow rate also indicates that a secondary oscillation of much lower frequency is present. This flow frequency oscillation seems to be associated with the unsteady behavior of the region of separated flow on the blade suction surfaces. The quasi-periodic nature of the flow separation is related to the vortex shedding from the blade. The physical interpretation of this phenomenon is that the vortex forms on the blade suction surface and grows as it migrates along the surface in the streamwise direction. This results in growth of the separation which acts as a blockage in the blade passage. This blockage then reduces the mass flow through the blade passage in an oscillatory fashion corresponding to the vortex shedding frequency. Figure 7 also shows a comparison between the time averaged non-steady mass flow rate and the circumferentially mass-averaged uniform inflow into the rotor. It is significant that the time averaged non-steady mass flow is about 5 percent higher than the mass averaged uniform inflow.

The magnitude of the flow separation is much larger than that observed in previous studies^{4,5}, as is the amplitude of the mass flow fluctuation due to the wakes entering the blade passage. Thus, it is believed that the influence of turbulence effects are not adequately taken into consideration with this formulation. Therefore, a turbulence model was incorporated into the computational procedure in regions near the blade surfaces in order to account for these effects. The turbulence model used in these computations is the algebraic eddy viscosity model of

Baldwin and Lomax. The incorporation of any turbulence model must be accomplished with extreme caution since they were developed for steady flow. Hence, improper implementation can result in suppression of the unsteady flow features.

The oscillatory mass flow for the turbulent computation is shown in Figure 8. In comparing this figure with the laminar results (Figure 7), it is seen that the amplitude of the oscillation due to the incoming wakes has been reduced substantially. It also appears that the low frequency oscillation associated with the vortex shedding has been suppressed as well. Also in this figure the time-averaged non-steady mass flow rate is compared with the mass flow computed for a uniform inflow corresponding to the circumferentially mass-averaged rotor inflow. Note that as in the laminar case the time averaged non-steady mass flow rate is higher than the corresponding thermodynamically equivalent steady flow, although the difference is only about three percent when the turbulence model is included compared to 5 percent in the laminar case.

Further insight can be gained by examining other flow properties. The extent of the separation for the laminar computation with unsteady inflow boundary conditions is shown in velocity vectors in Figure 9. A careful examination of this flow separation reveals the formation of the vortex on the suction surface. This vortex is ultimately shed and migrates through the blade wake region in the direction opposite to the rotation of the blades. Figure 10 shows velocity vectors for the unsteady flow using the Baldwin-Lomax turbulence model in the computation. These velocity vectors show that the incorporation of the turbulence model diminishes the extent of the flow separation significantly. In fact, the region which was separated in the laminar computation has become primarily a region of very low-speed flow with only a small separation occurring very near the trailing edge of the blade on the suction surface. Although much smaller than in the laminar case, a vortex is shed from the

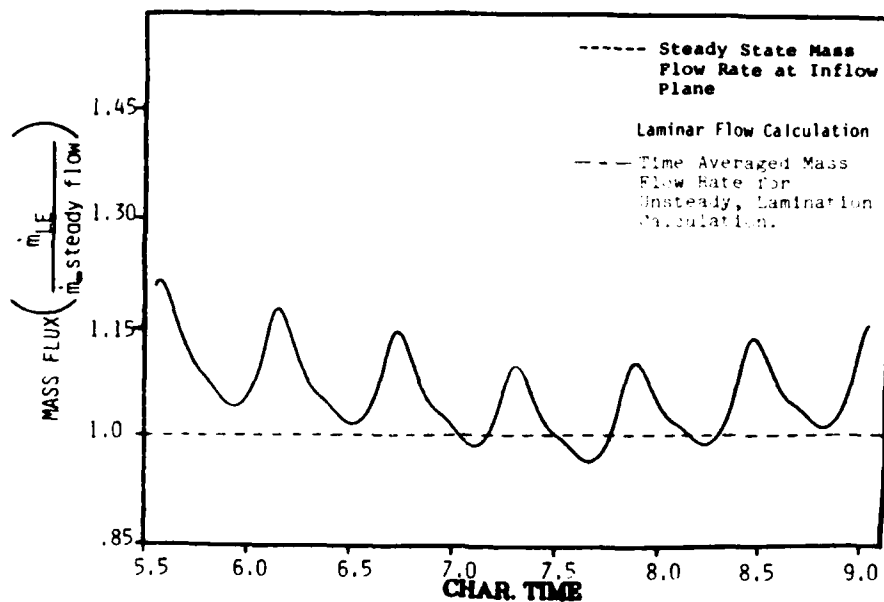


Figure 7. Comparison of time-dependent mass flow and steady state mass flow at blade leading edge - laminar calculation.

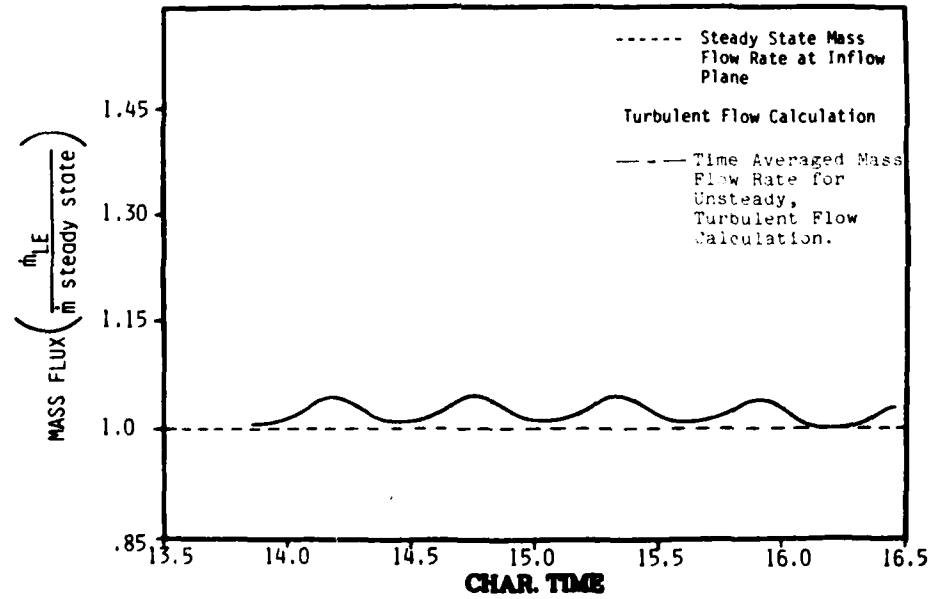


Figure 8. Comparison of time-dependent mass flow and steady state mass flow at blade leading edge - turbulent calculation.

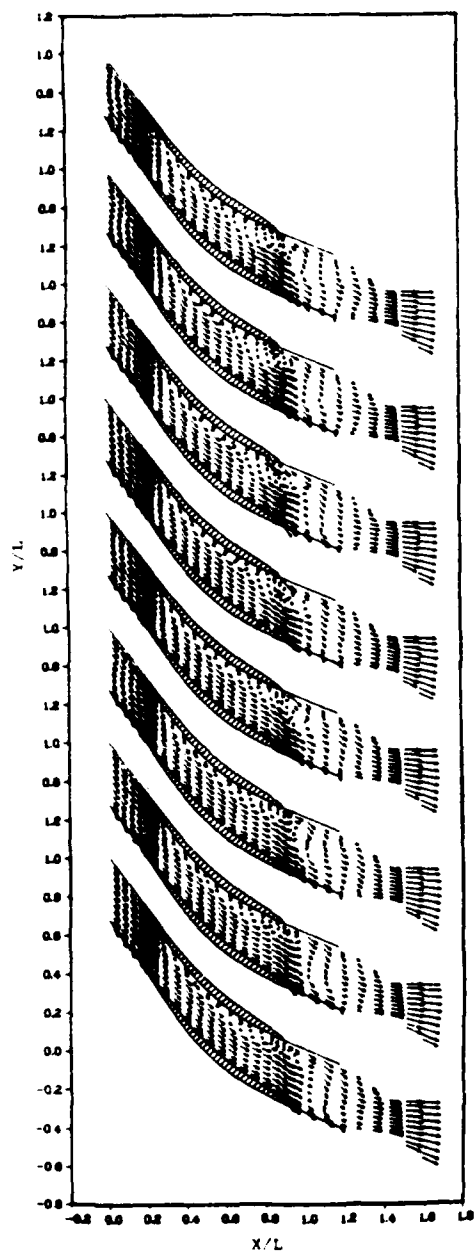


Figure 9. Velocity vectors for laminar computation.

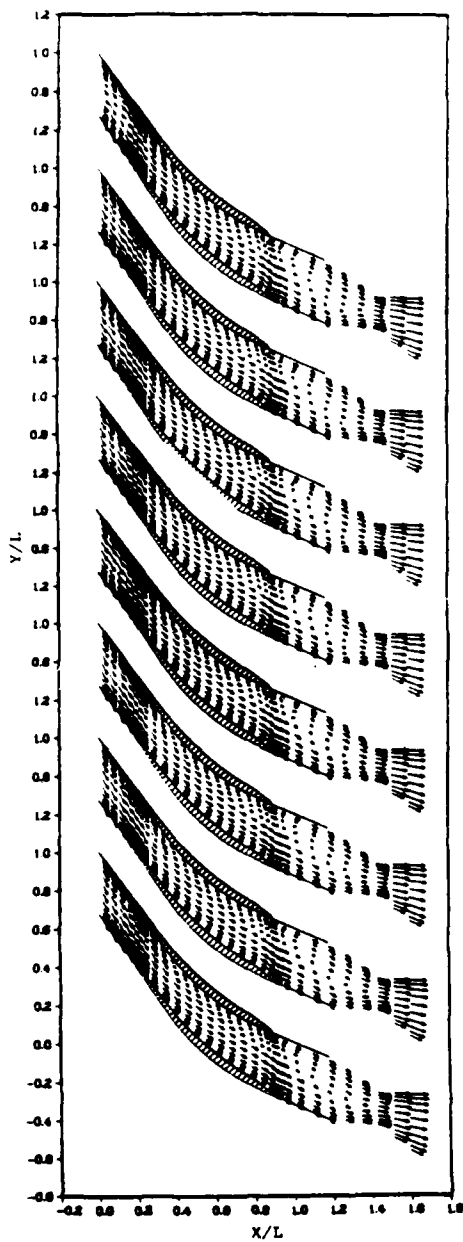


Figure 10. Velocity vectors for turbulent computation.

trailing edge and migrates through the wake region in much the same fashion as for the laminar computation.

The Mach contours also display a number of the unsteady flow features. From the results of Reference 7, the Mach number contours show the oscillatory behavior of the oblique shock wave at the blade leading edge (Figure 11). Also this figure shows that the shock wave impinges on the suction surface boundary layer in the region where the onset of separation seems to occur. The oscillatory growth and decay of the separation near the blade trailing edge is also seen in this figure. Comparison with the velocity vector plots shows this behavior is associated with the formation and shedding of the vortex structure. The Mach number contours for the computations with turbulence included are shown in Figure 12. The time-dependent behavior shown in this figure indicates that the turbulence model reduces the strength of the leading-edge shock and the extent of flow separation. In addition, note that the oscillatory nature of the flow separation is reduced significantly in amplitude by including the turbulence model. The large fluctuations in the flow for the laminar case are shown in the time varying blade surface pressure distributions (Figure 13). Again the large amplitude in pressure fluctuation at the blade trailing edge is associated with the vortex shedding phenomena. This figure also reveals a large spike in the static pressure on both the pressure and suction surfaces at the blade leading edge. This is the result of numerically smearing the shock so that it behaves as a detached bow shock in which the pressure tends toward the stagnation value on the pressure surface. The flow then rapidly expands around the leading edge on both surfaces and the pressure recovers toward the value which would be produced by a weak attached shock on the pressure surface. This phenomena is smeared over a much larger region than would be expected in an actual physical flow due to the relatively coarse grid in the vicinity of the blade leading edge. This oblique shock wave then impinges on the suction surface of the adjacent blade causing boundary layer separation in a classical

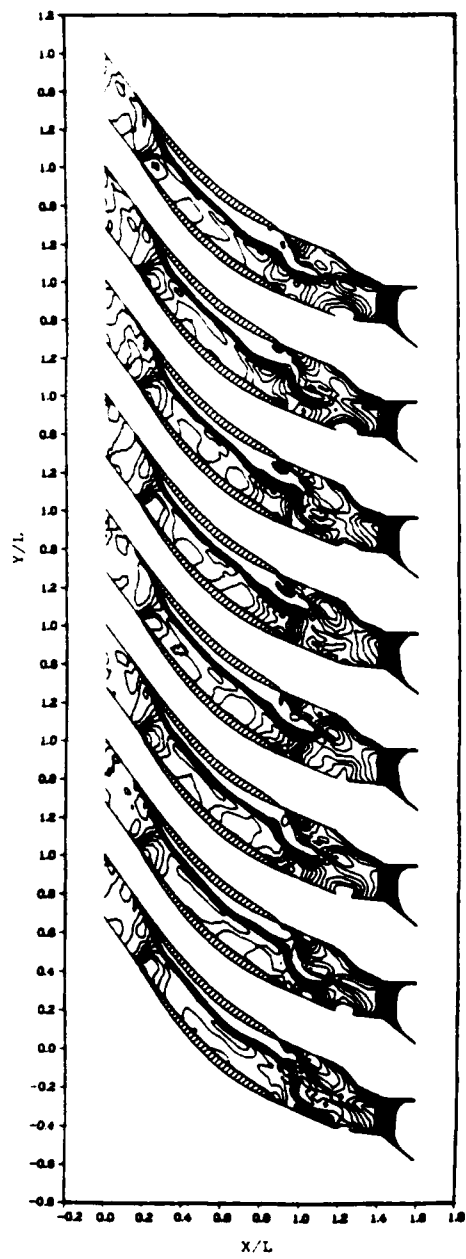


Figure 11. Mach contours for laminar computation.

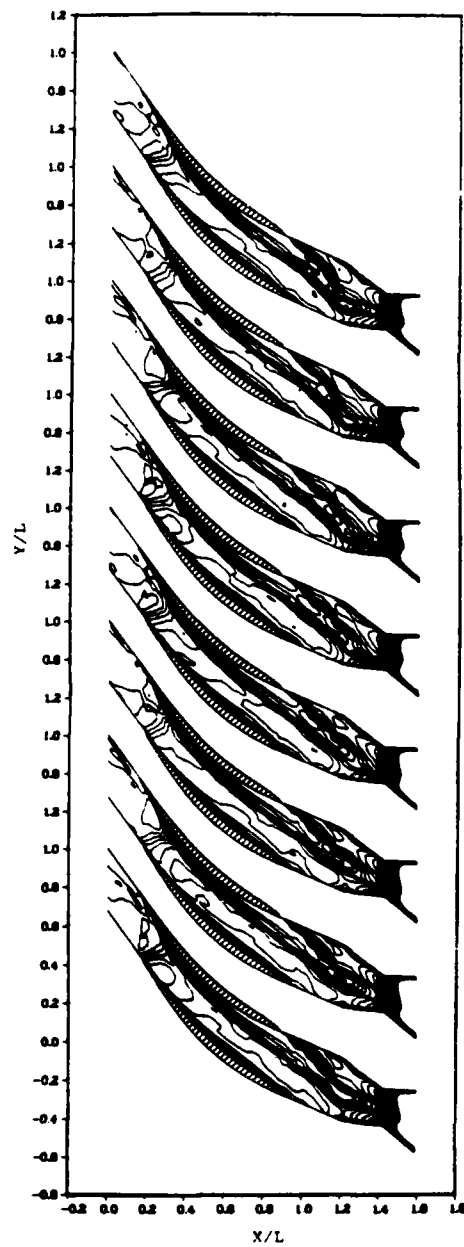


Figure 12. Mach contours for turbulent computation.

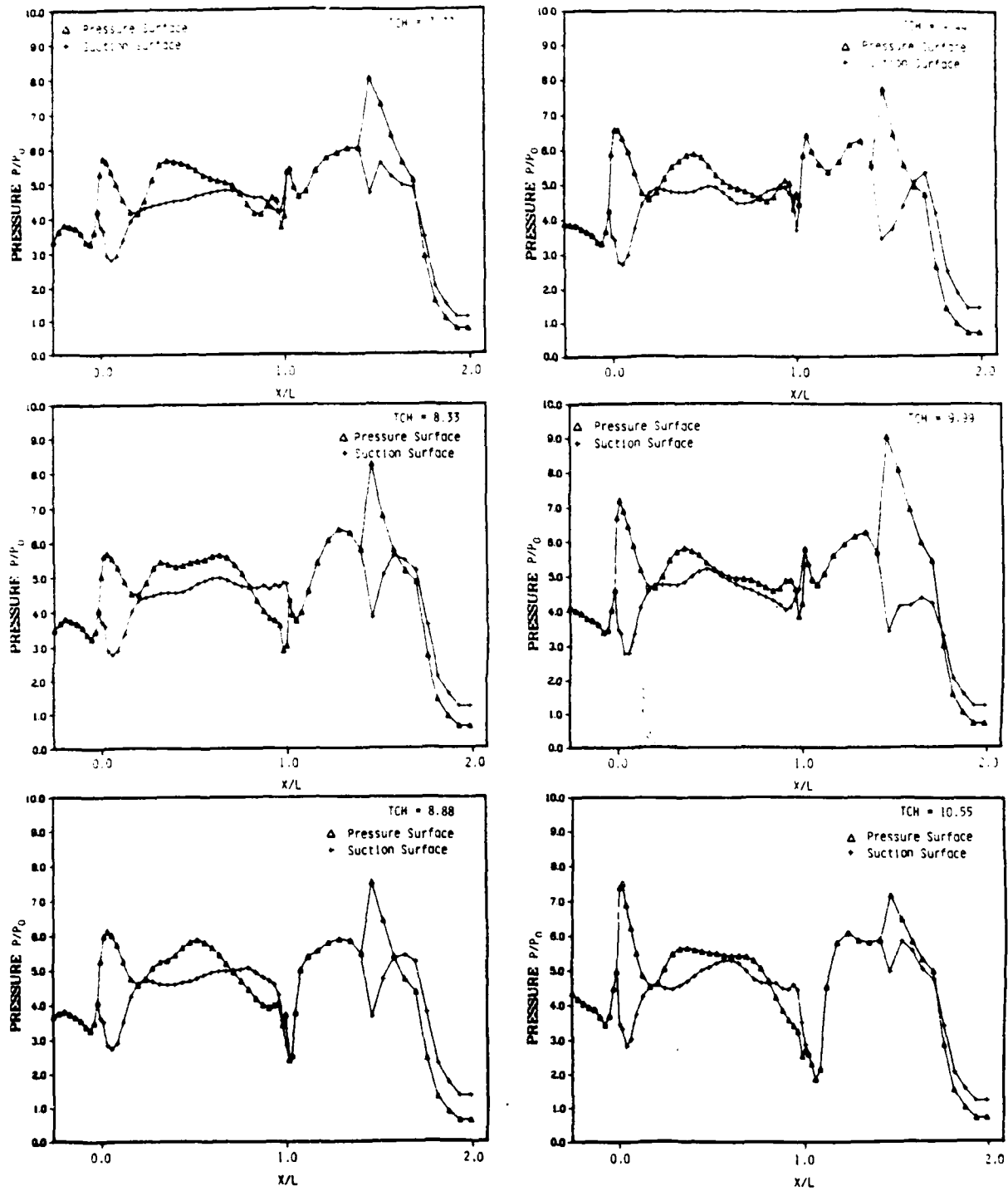


Figure 13. Blade surface pressure variation with time: laminar case.

shock wave--boundary layer interaction. The wave is then reflected back toward the pressure surface causing a subsequent rise in the surface pressure. The drop in static pressure on the suction surface shows the presence of the expansion just inside the blade passage. Again comparing with the surface static pressure distribution for the turbulent calculation we observed that the magnitude of the fluctuations are reduced significantly (Figure 14). In particular, the large fluctuation at the trailing edge for the laminar case is almost completely eliminated. Referring to the velocity vectors (Figures 9 and 10), note that in the turbulent case the vortex strength at the trailing edge has been reduced to nearly zero in the turbulent computations. Also note that the sharp spike near the leading edge of the pressure surface has been eliminated, supporting the previous observation that the shock strength had been reduced in the turbulent calculations.

Examination of the stagnation pressure contours for both the laminar (Figure 15) and turbulent (Figure 16) computations is revealing. For the laminar case the periodic behavior repeats at the blade leading edge at approximately 0.55 characteristic time while the behavior at the trailing edge is not repeatable due to the oscillatory behavior of the flow separation. In the case of the turbulent flow the periodic behavior at the leading edge also repeats at about 0.55 characteristic time. However, note for this case that this periodicity is essentially preserved throughout the blade passage. This is attributed to the fact that the turbulence model suppresses the oscillatory behavior of the flow separation region. The time variation of stagnation pressure can be regarded as entropy waves migrating through the blade passage. Viewing the stagnation pressure in this fashion gives a good view of the time history of the wakes from the upstream components.

Computation for Multiple Blade Passages

Although the computation of time-dependent flow through a single blade passage provides significant insight into many aspects of the unsteady flow in the compressor rotor, this

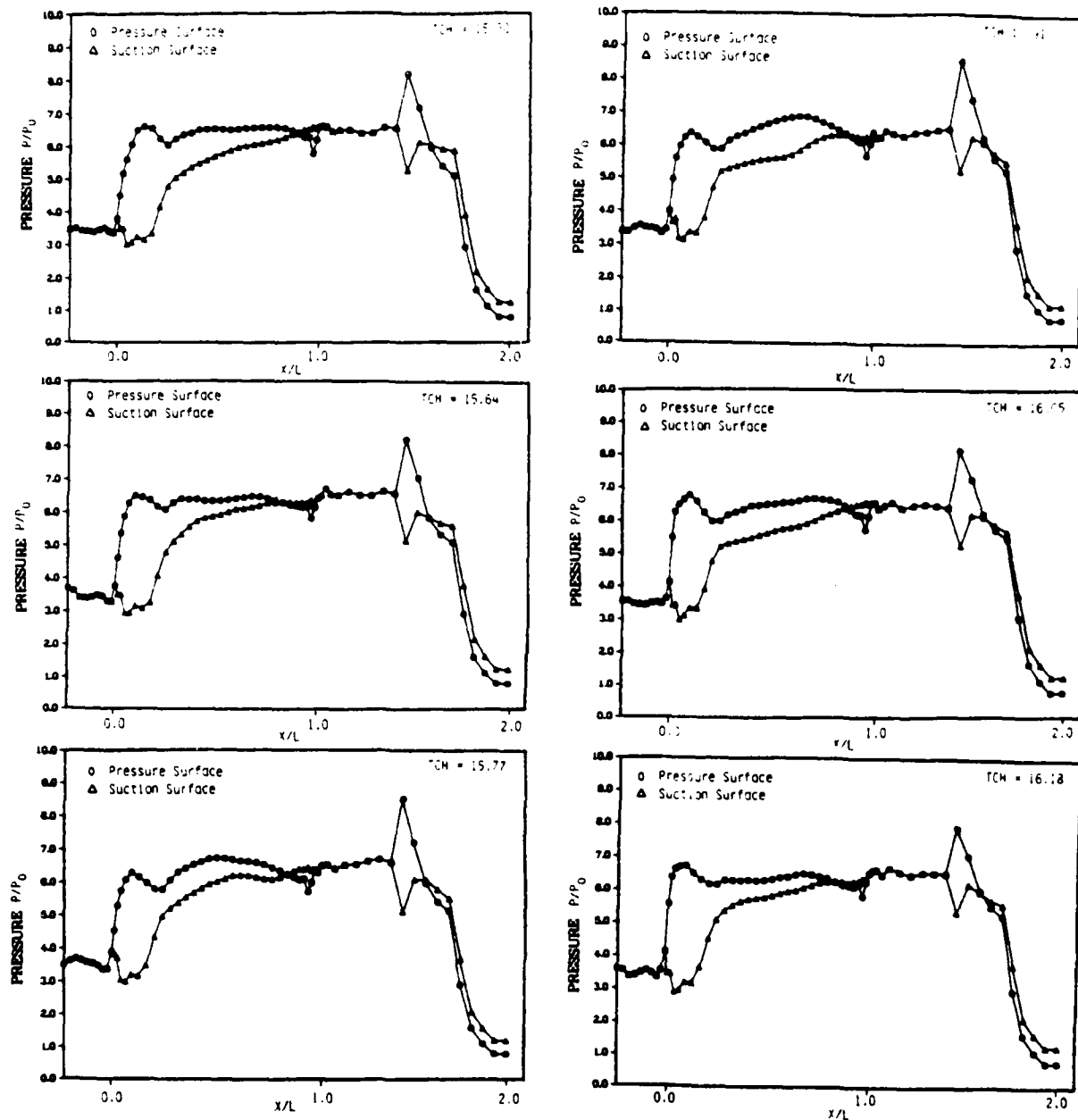


Figure 14. Blade surface pressure variation with time: turbulent case.

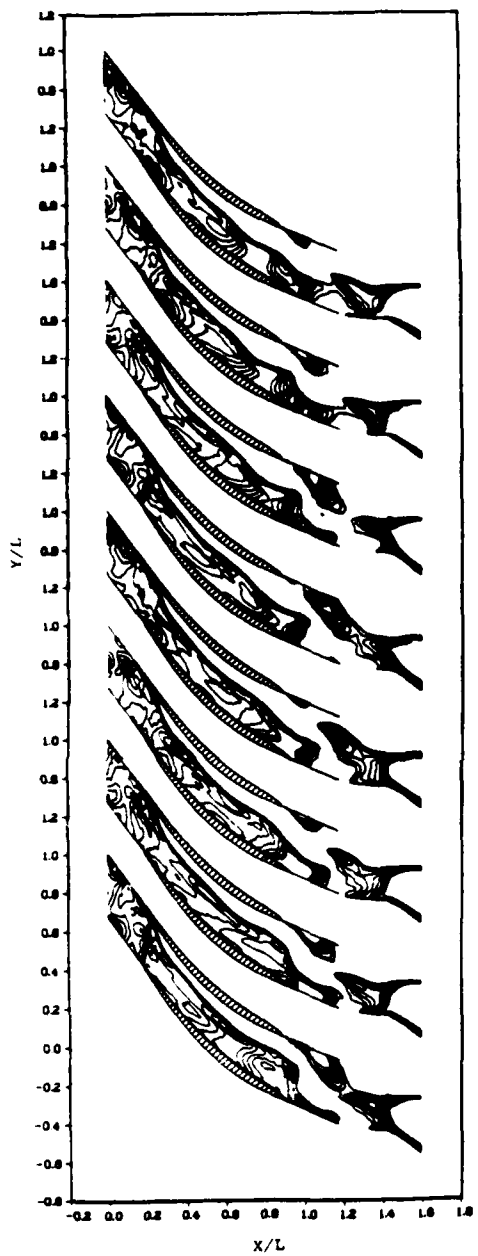


Figure 15. Stagnation pressure for laminar computation.

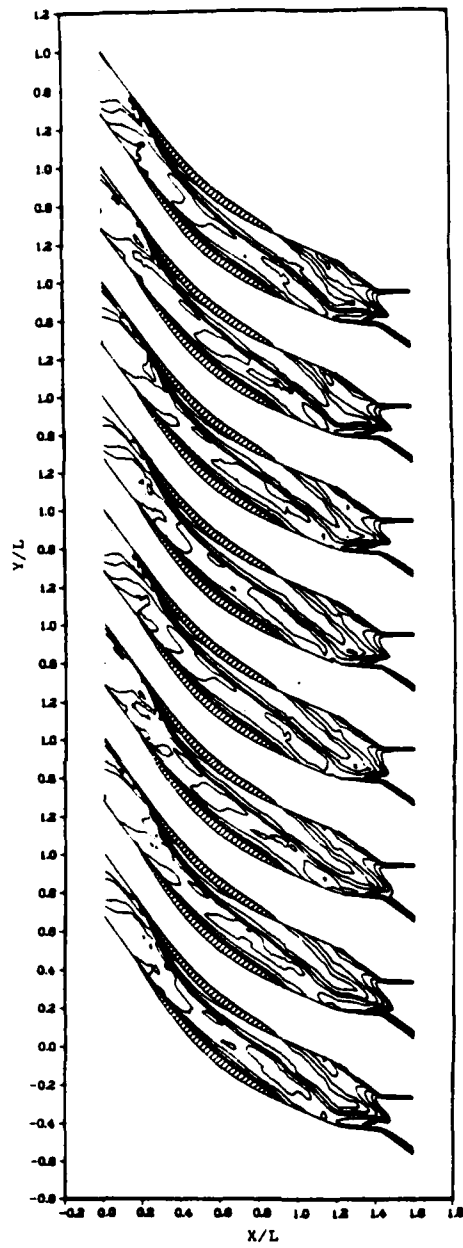


Figure 16. Stagnation pressure for turbulent computation.

simulation does not adequately represent the details of the periodic nature of the flow. In order to simulate the periodic behavior exactly it would be necessary to compute the flow through at least half of the rotor (i.e., 37 blades) since the ratio of stator to rotor blades is 54:74. Since current computer storage is not sufficient to accommodate a time accurate computation of this magnitude the real configuration is approximated by computing the flow through three blade passages, assuming three upstream stator blades for every four rotor blades. The computed results for this configuration much more closely simulate the actual compressor flow than the computations for the single blade passage.

The computation for three blade passages was accomplished by first expanding the grid to this configuration and then performing the calculations for laminar flow with the steady inflow boundary conditions. After a stable solution was obtained, the time-dependent inflow boundary conditions were imposed to account for the wakes from upstream components. The results for this computation give a better indication of how time dependent features vary between blade passages (than in the single blade passage case). Figures 17a, b, c, and d represent typical examples of Mach number, static pressure, stagnation pressure and velocity vectors for the laminar steady in flow case. It is believed that more accurate simulations are achieved by incorporating the Baldwin Lomax turbulence model. The effect of this again was suppression of the magnitude of the unsteady flow features.

To examine the influence of the unsteady flow separation on the blade suction surface, computations were performed for several characteristic times with steady inflow boundary conditions. Figure 18 shows the time varying mass flow at the blade leading edge for this case. The oscillatory behavior of the mass flow rate is associated with the quasi-periodic fluctuations in the flow separation on the blade suction surface. As noted previously this is related to the vortex shedding at the blade trailing edge.

MACH NO. - T=.1927728E-1

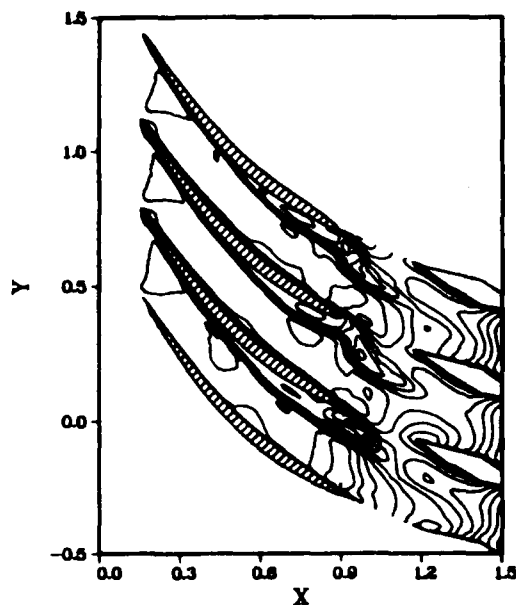


Figure 17a. Typical computed mach number contours.
Laminar, steady inflow boundary condition test case.

STAT PRESS - T=.1927728E-1

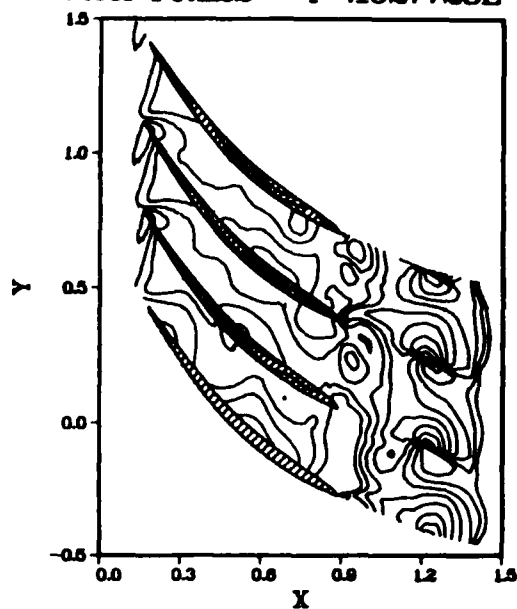


Figure 17b. Typical computed static pressure contours.
Laminar, steady inflow boundary condition test case.

STAG PRESS - T=.1927728E-1

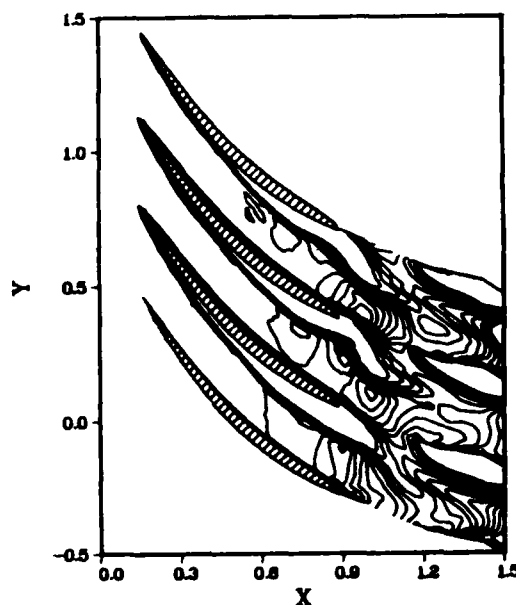


Figure 17c. Typical computed stagnation pressure contours.
Laminar, steady inflow boundary condition test case.

VEL. VECTORS - T=.1927728E-1

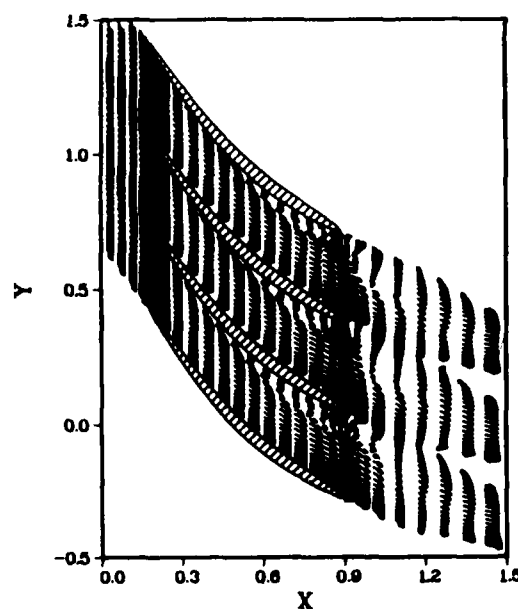


Figure 17d. Typical computed velocity vectors.
Laminar, steady inflow boundary condition test case.

MASS FLOW VS. TIME

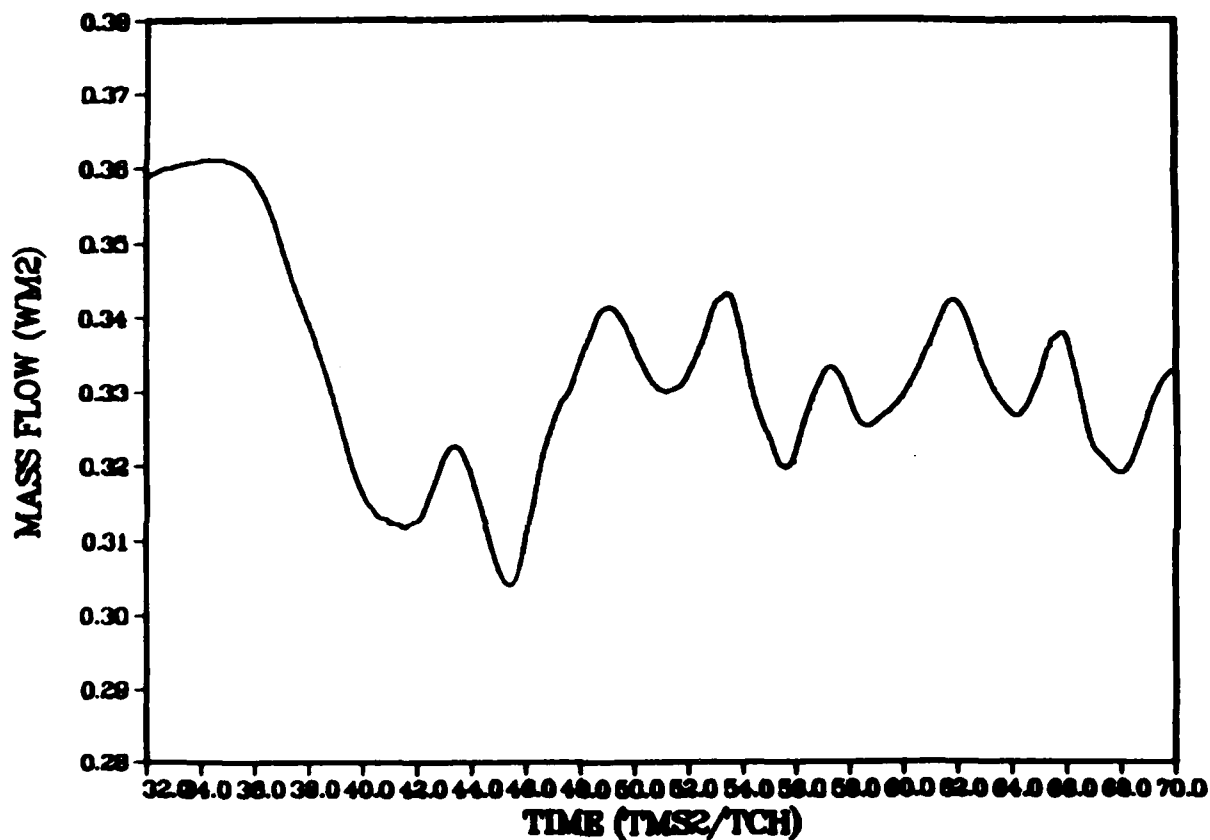


Figure 18. Mass flow rate at blade leading edge. Steady inflow boundary conditions.

Careful examination of this oscillatory flow separation reveals that it migrates from one blade row to the next. Although this behavior is somewhat reminiscent of rotating stall, it occurs at a much higher frequency than would be expected in an actual rotor. This can be attributed to fact that the periodic boundary conditions are imposed over only four blades. Consequently, the disturbance can only migrate through three blade passages before it repeats while in the actual rotor it may travel around the full circumference. Since the flow separation is strongly coupled to the adverse pressure gradient across the blade row, the magnitude of this separation and the resultant flow blockage were reduced by decreasing the pressure ratio across the blade row. This was accomplished by increasing the throat area of the downstream choke nozzle through a series of numerical experiments. From the numerical experiment it was found that increasing the downstream nozzle area to correspond to an area ratio of $A/A^*_2 \sim 0.65$ eliminates the migration of the flow separation from one blade passage to another. The influence of varying the nozzle area ratio on the mass flow rate is shown in Figure 19. The variation of absolute stagnation pressure ratio across the rotor as a function of nozzle area is shown in Figure 20. As indicated in these figures the mass flow rate and the stagnation pressure ratio behave somewhat erratically for nozzle area ratios at which the unsteady separation is present. Figure 21 shows the variation of absolute stagnation pressure with mass flow rate. The results of the numerical experiment are summarized in Table 2.

Upon elimination of the unsteady flow separation, the time-dependent inflow boundary conditions were once again incorporated into the computation. The mass flow rate at the blade leading edge is shown both with these boundary conditions and with the steady inflow boundary conditions in Figure 22. For the steady inflow, the mass flow rate is 0.362 slugs/(sec-ft) while the

MASSFLOW VS. NOZZLE AREA RATIO

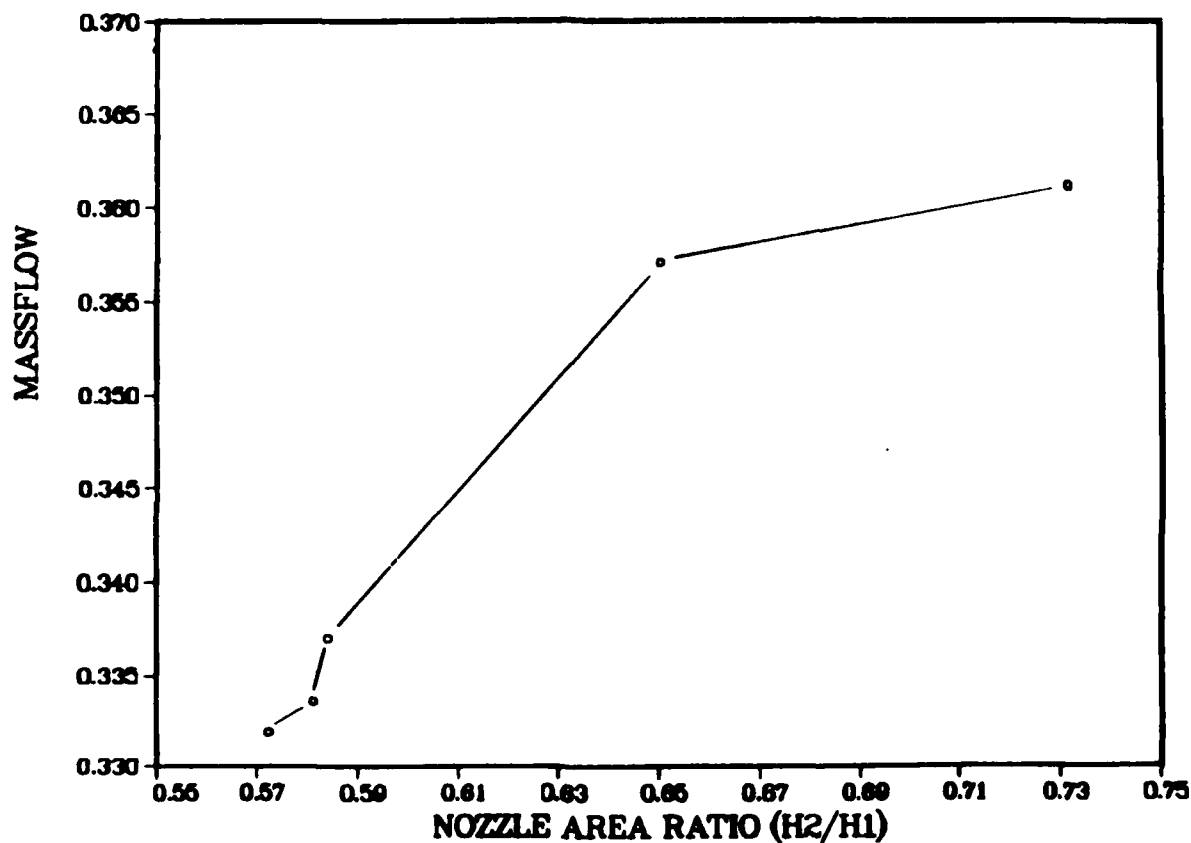


Figure 19. Computed mass flow rate as a function of exit nozzle area ratio.

ABSOLUTE STAGNATION PRESSURE RATIO VERSUS MASS FLOW

STAG PRESS RATIO VS. NOZZLE AREA RATIO

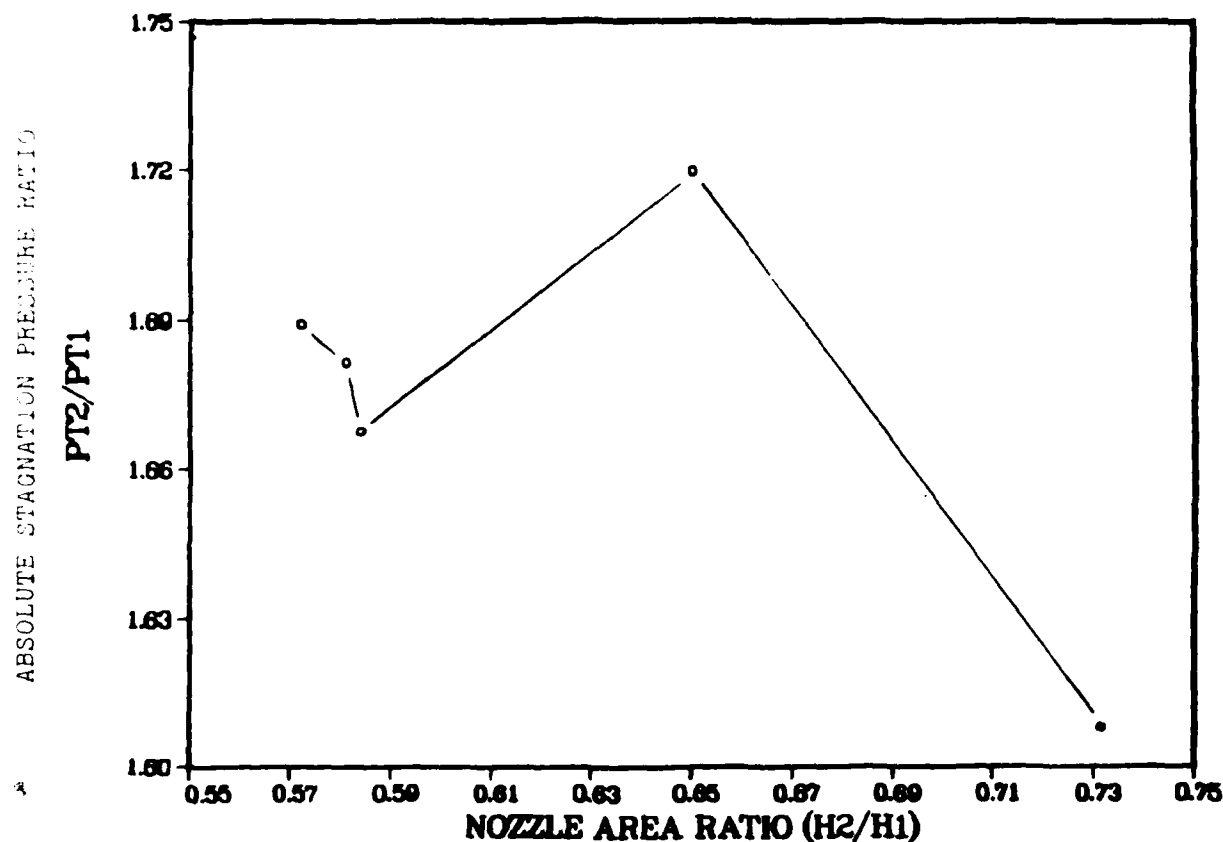


Figure 20. Computed stagnation pressure ratio as a function of exit nozzle area ratio.

STAG PRESS RATIO VS. MASSFLOW

ABSOLUTE STAGNATION PRESSURE RATIO VERSUS MASS FLOW

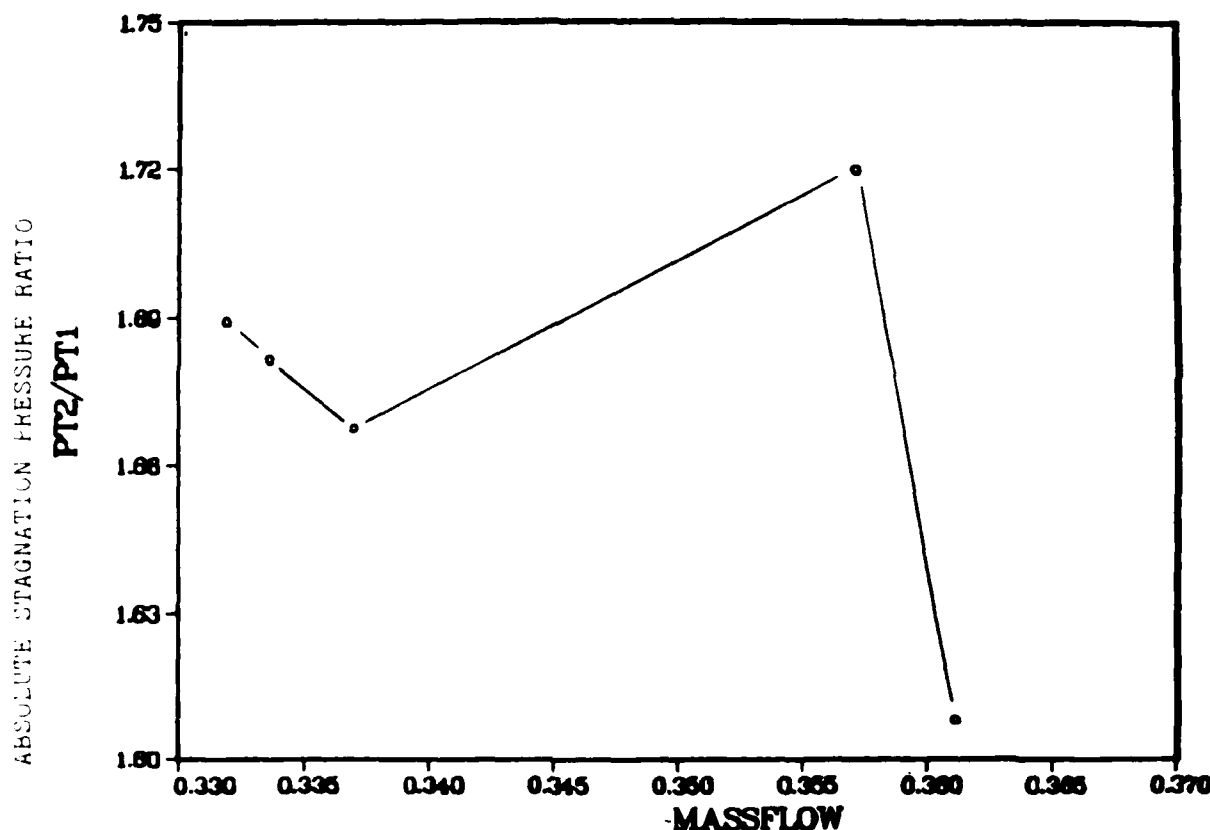


Figure 21. Variation in stagnation pressure ratio as a function of mass flow rate.

TABLE 2. SUMMARY OF EXIT NOZZLE AREA RATIO STUDY.

EXIT NOZZLE AREA RATIO	AVERAGE MASS FLOW RATE (SLUGS/S)	ABSOLUTE STAGNATION PRESSURE RATIO (P_{Te}/P_{Ti})	FREQUENCY OF OSCILLATIONS CYCLE/CHAR. TIME
0.5772	0.332	1.689	0.250
0.5811	0.334	1.682	0.250
0.5840	0.337	1.668	0.222
0.6501	0.357	1.720	0.083
0.7314	0.361	1.608	0.000

MASS FLOW VS. TIME

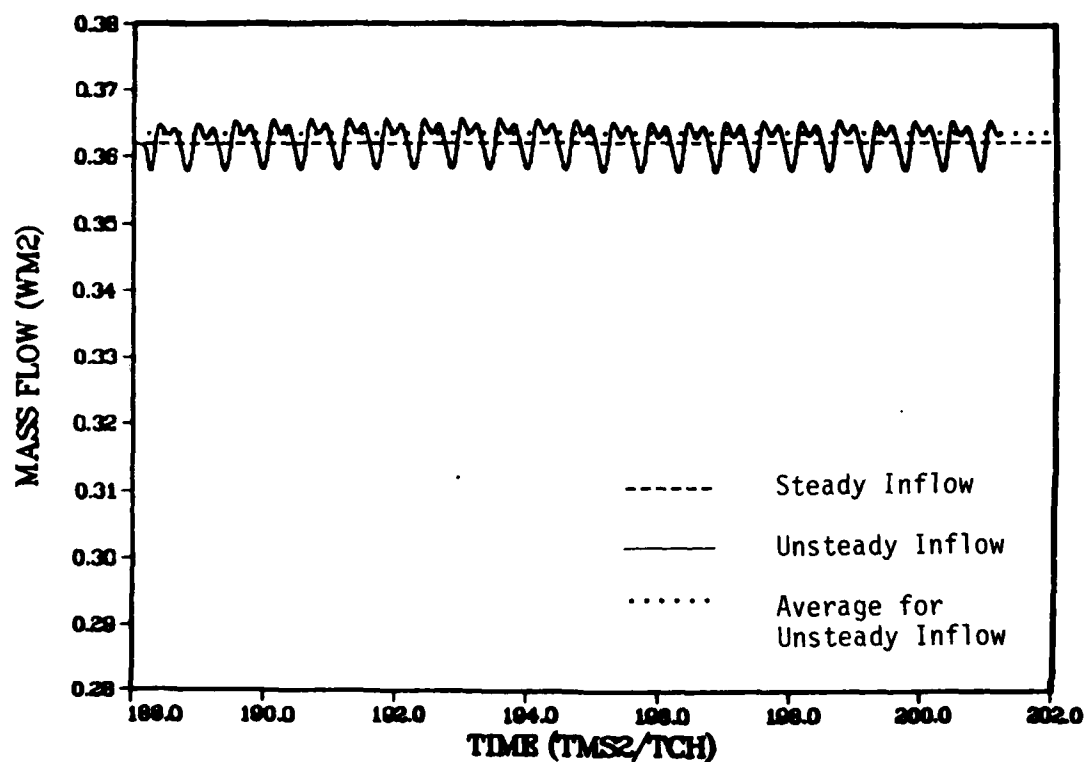


Figure 22. Computed mass flow rate. Steady and unsteady inflow boundary conditions.

average mass flow rate for the unsteady inflow is 0.364 slugs/(sec-ft). Although the unsteady value is slightly higher (less than 1%), the difference between the two is much smaller than that observed for higher pressure ratios across the blade row. For higher pressure ratios the unsteady inflow produced an average mass flow in excess of 3% higher than that for steady inflow. The reduction in this difference with pressure ratio implies that the oscillatory unsteady inflow is not the sole source of the higher mass flow rate. It should also be noted that the overall average level of the mass flow increases as the absolute stagnation pressure ratio across the blade row is decreased. Additional details of the flow for this configuration are seen by examining the Mach number contours, static and stagnation pressure contours and velocity vectors as they vary with time. These flow properties are shown in Figures 23, 24, 25, and 26, respectively.

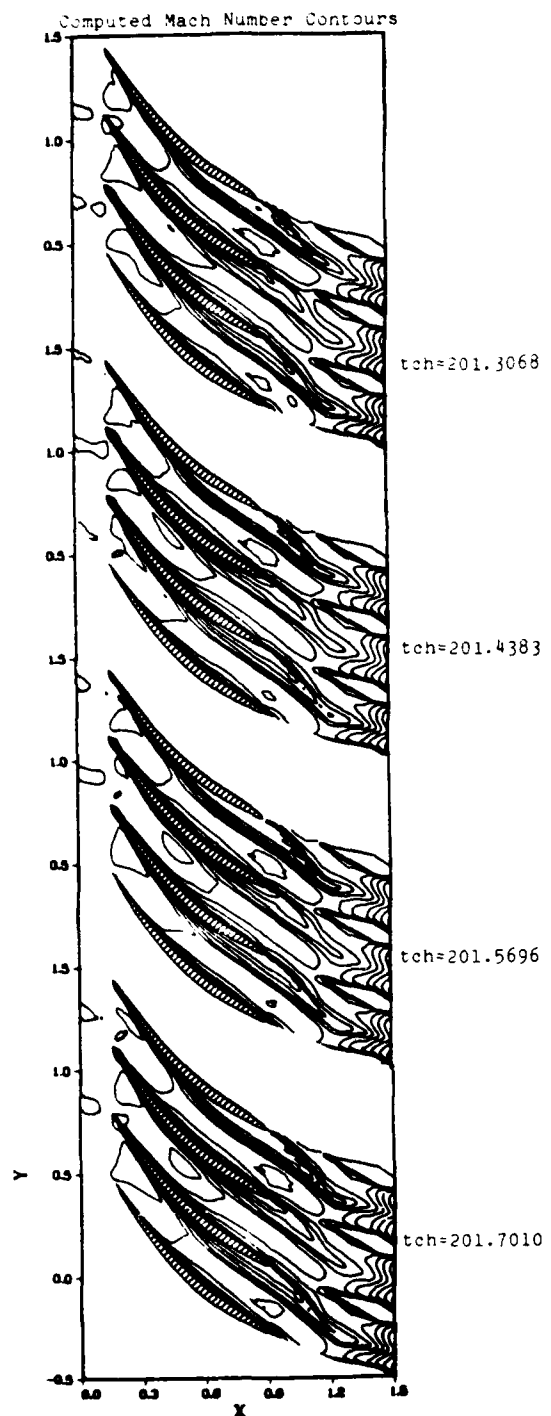


Figure 23. Computed mach numbers at several characteristic times. Time-dependent inflow boundary conditions.

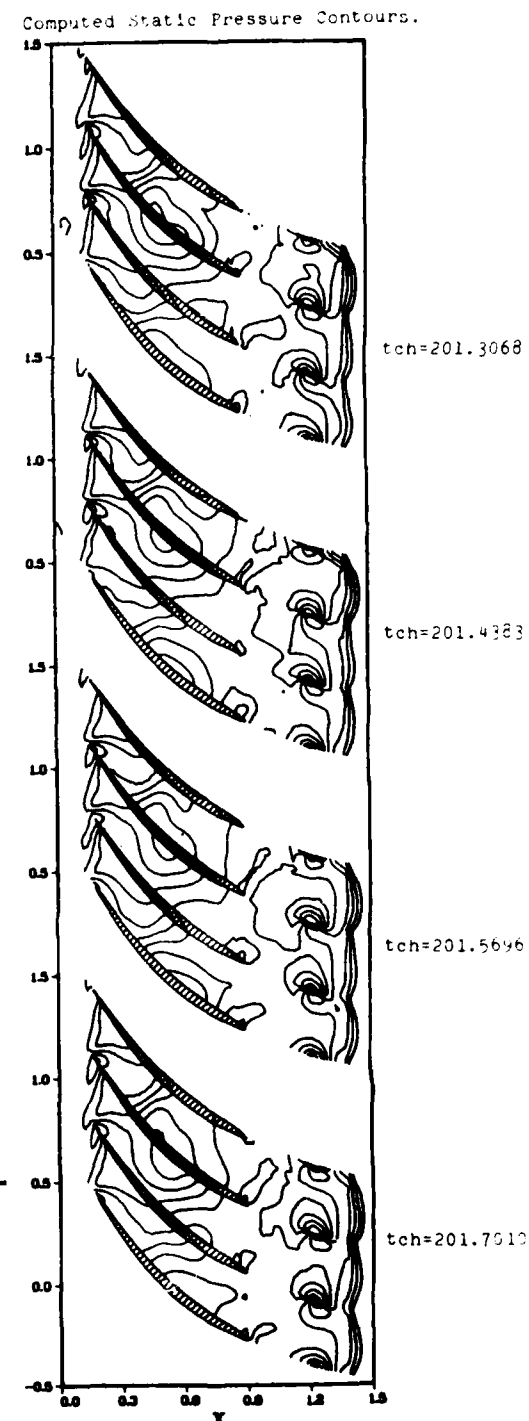


Figure 24. Computed static pressure contours at several characteristic times. Time-dependent inflow boundary conditions.

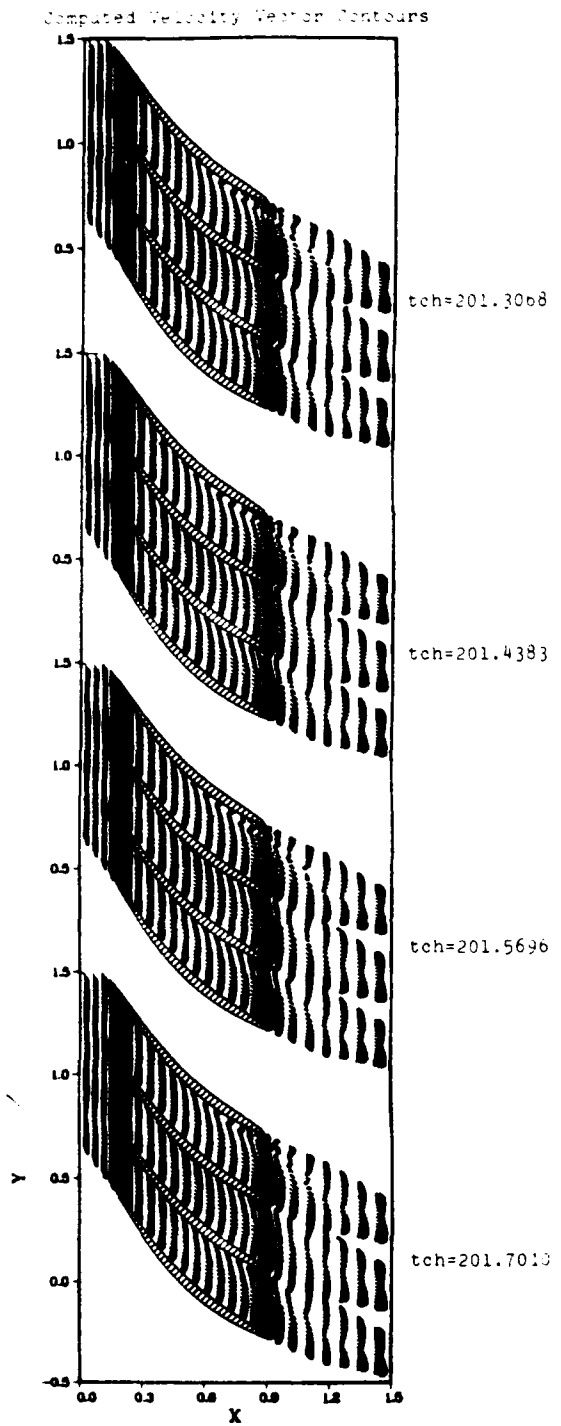


Figure 25. Computed stagnation pressure contours at several characteristic times. Time-dependent inflow boundary conditions.

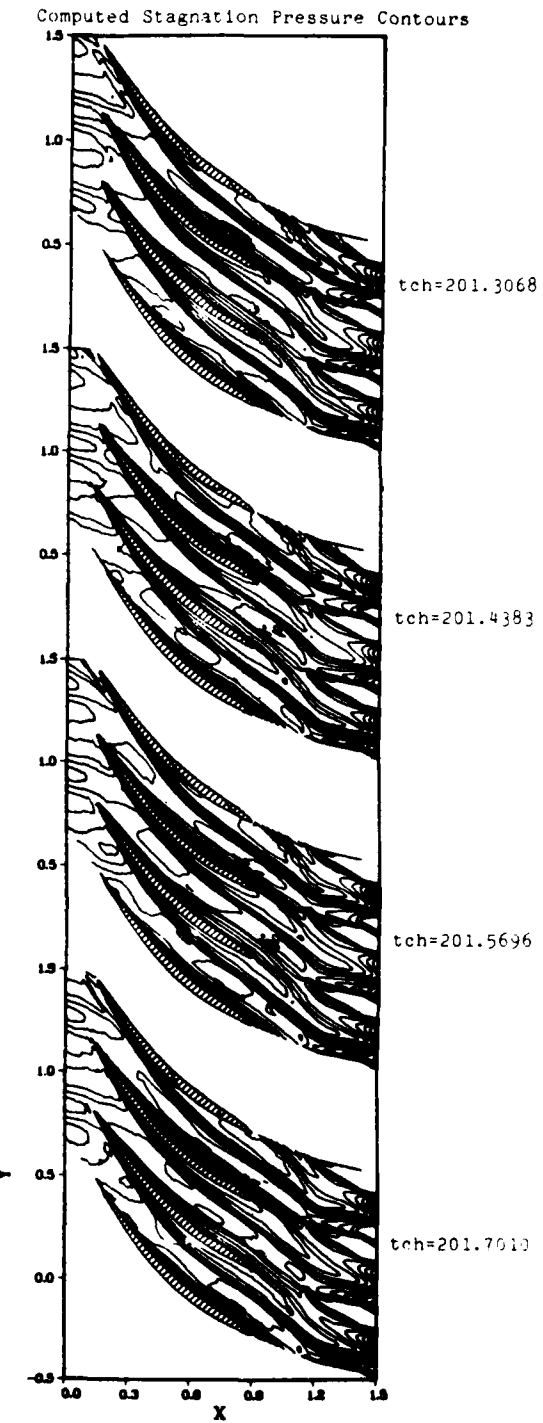


Figure 26. Computed velocity vectors at several characteristic times. Time-dependent inflow boundary conditions.

SECTION V CONCLUSIONS AND RECOMMENDATIONS

Procedures have been developed for treating boundary conditions for a supersonic flow entering a two-dimensional compressor rotor blade row and a subsonic flow exiting that blade row. The upstream boundary conditions are formulated using characteristic variables and an experimentally measured stagnation pressure profile to simulate the pressure and velocity defects from the wake of upstream stators and inlet guide vanes. This formulation also produces the proper entropy variation at the inflow boundary. The downstream boundary conditions are developed by incorporating a "second throat" (A_2^*) downstream of the blade trailing edge and imposing supersonic outflow boundary conditions at the exit of the throat. The area of the "second throat" can be adjusted to relocate the shock and the pressure rise across the blade passage. The computation also incorporates streamtube contraction through the axial component of the continuity equation to allow for some three-dimensional effects. These boundary conditions are used to obtain solutions to the complete time-dependent compressible Navier-Stokes equations for the transonic compressor rotor. A series of four rotor blades with three stator wakes are computed with periodicity imposed. This represents the periodic behavior of a stage with 74 rotor blades and 54 stator blades.

Both laminar and turbulent cases are computed. Results are presented in the form of velocity vectors, Mach and total pressure contours, blade surface pressure distribution and mass flow history. The computed results give a good representation of the time varying flow properties in a compressor rotor and provide a significant advance in solving the time-dependent viscous flow field in turbomachinery.

Recommendations are:

- a. Decrease region of bow shock influence.
- b. Resolve shock reflection region.
- c. Improve turbulence model for unsteady cases.
- d. Investigate three-dimensional effects.
- e. Examine rotor-stator interaction.

REFERENCES

1. Mitchell, N. A., A Time Marching Method for Unsteady Two Dimensional Flow in a Blade Passage, CUED/A-TURBO/TR 100, Cambridge University, 1980.
2. Hodson, H. P., "An Inviscid Blade-to-Blade Prediction of a Wake-Generated Unsteady Flow," ASME Paper 84-GT-43, June 1984.
3. Denton, J. D., "An Improved Time-Marching Method for Turbomachinery Flow Calculation," ASME Paper 82-GT-239, Journal of Engineering for Power, Vol. 105, July 1983.
4. Janssens, P. and Hirsch, C., "A Viscid-Inviscid Interaction Procedure for Two Dimensional Cascades," Viscous Effects in Turbomachines, AGARD CP 351, June 1983.
5. Calvert, W. J., "Application of an Inviscid-Viscous Interaction Method to Transonic Compressor Cascades," Viscous Effects in Turbomachines, AGARD CP 351, June 1983.
6. Rai, M. M., "Navier-Stokes Simulations of Rotor-Stator Interaction Using Patched and Overlaid Grids," AIAA Paper 85-1519, July 1985.
7. Scott, J. N. and Hankey, W. L., "Boundary Conditions for Navier-Stokes Solutions of Unsteady Flow in a Compressor Rotor," Three-Dimensional Flow Phenomena in Fluid Machinery, Fluids Engineering Technical Session, Vol. 32, Published volume of the ASME 1985 Winter Annual Meeting, November 1985.
8. Shang, J. S., "Oscillatory Compressible Flow Around a Cylinder," AIAA Paper 82-0098, Paper presented at AIAA 20th Aerospace Sciences Meeting, Orlando, Florida, 11-14 January 1982.
9. Shang, J. S., "Numerical Simulation of Wind-Fuselage Aerodynamic Interaction," AIAA Paper 83-0225, Paper presented at AIAA 21st Aerospace Sciences Meeting, Reno, Nevada, 10-13 January 1983.
10. Scott, J. N. and Hankey, W. L. Jr., "Numerical Simulation of Cold Flow in an Axisymmetric Centerbody Combustor," AIAA Paper 83-1741, Paper presented at AIAA 16th Fluid and Plasma Dynamics Conference, Danvers, Massachusetts, 12-14 July 1983.
11. Steger, J. L., Pulliam, T. H., and Chima, R. V., "An Implicit Finite Difference Code for Inviscid and Viscous Cascade Flow," AIAA Paper 80-1427, Paper presented at AIAA 13th Fluid & Plasma Dynamics Conference, Snowmass, Colorado, July 14-16, 1980.

12. Chima, R. V., "Analysis of Inviscid and Viscous Flows in Cascades with an Explicitly Multiple grid Algorithm," AIAA Paper 84-1663, June 1984.
13. Gopalakrishnan, S. and Bozzola, R., "Computation of Shocked Flows in Compressor Cascades," ASME Paper 72-GT-31.
14. Scott, J. N., "Numerical Simulation of Unsteady Flow in a Compressor Rotor Cascade," AIAA Paper 85-0133, Paper presented at AIAA 23rd Aerospace Sciences Meeting, Reno, Nevada, January 14-17. 1985.
15. McKenna, P. J., Graham, J. E., and Hankey, W. L., The Role of Far-Field Boundary Conditions in Numerical Solutions of the Navier-Stokes Equations, AFWAL-TR-82-3029, Air Force Wright Aeronautical Laboratories, Wright-Patterson Air Froce Base, Ohio, September 1982.
16. Erdos, J. I. and Alzner, E., "Computation of Unsteady Transonic Flows Through Rotating and Stationary Cascades," N.A.S.A. CR-2900, 1977.
17. Baldwin, B. S. and Lomax, H., "Thin Layer Approximation and Algebraic Model for Separated Turbulent Flows," AIAA Paper 78-257, January 1978.
18. MacCormack, R. W., "Numerical Solution of the Interaction of a Shock Wave with a Laminar Boundary Layer," Lecture Notes in Physics, Springer-Verlag, Vol. 59, 1971.

NOMENCLATURE

c	speed of sound
e	specific energy
E,F	vector fluxes in mean flow equations
i,j	indices for grid point location
k	thermal conductivity
K _i	characteristic variables
L	characteristic length (blade chord)
n	time index
p	pressure
R	gas constant, radius
t	time
T	temperature
U	dependent variable
u,v	velocity components
w	wheel speed
x	axial coordinate
y	tangential coordinate
α	stator flow angle
β	damping factor
γ	ratio of specific heats
δ	streamtube contraction factor
ζ, η	transformed coordinates
θ	azimuthal angle
λ	-2/3 μ , second viscosity coefficient
μ	molecular viscosity coefficient
ρ	density
σ_{xx}, σ_{yy}	normal stresses
τ_{xy}	shear stress
ω	vorticity

NOMENCLATURE (Continued)

Subscripts

∞	free stream (annulus) condition
w	wall condition
JL _{max}	maximum value
KL _{min}	minimum value
L	lower surface
o	stagnation value
s	stator coordinate frame
u	upper surface

END

DATE

FILMD

3 - 88

DTIC